Peng, Guotao ; He, Yuan ; Wang, Xiaoxiao ; Cheng, Yan ; Zhang, Haiyuan ; Savolainen, Kai ; Mädler, Lutz ; Pokhrel, Suman ; Lin, Sijie

Redox Activity and Nano–Bio Interactions Determine the Skin Injury Potential of Co3O4-Based Metal Oxide Nanoparticles toward Zebrafish

Journal Article	as:	peer-reviewed accepted version (Postprint)
DOI of this document*(secondary publication):		https://doi.org/10.26092/elib/3703
Publication date of this document:		19/02/2025

* for better findability or for reliable citation

Recommended Citation (primary publication/Version of Record) incl. DOI:

Redox Activity and Nano–Bio Interactions Determine the Skin Injury Potential of Co3O4-Based Metal Oxide Nanoparticles toward Zebrafish.
Guotao Peng, Yuan He, Xiaoxiao Wang, Yan Cheng, Haiyuan Zhang, Kai Savolainen, Lutz Mädler, Suman Pokhrel, and Sijie Lin. ACS Nano 2020 14 (4), 4166-4177
DOI: 10.1021/acsnano.9b08938

Redox Activity and Nano-Bio Interactions Determine the Injury Potential of Metal Oxide Nanoparticles towards Zebrafish

Guotao Peng[1,2], Yuan He[1,2], Xiaoxiao Wang[1,2], Haiyuan Zhang[3], Kai Savolainen[4], Lutz Mädler[5,6], Suman Pokhrel[5,6*], Sijie Lin[1,2*]

[1]College of Environmental Science and Engineering, Biomedical Multidisciplinary Innovation Research Institute, Shanghai East Hospital, Tongji University, 1239 Siping Road, Shanghai 200092, China;
[2]Shanghai Institute of Pollution Control and Ecological Security; Key Laboratory of Yangtze River Water Environment, Ministry of Education, China;
[3]Laboratory of Chemical Biology, Changchun Institute of Applied Chemistry, Chinese Academy of Sciences, Changchun, Jilin 130022, China;
[4]Finnish Institute of Occupational Health, Helsinki, Finland;
[5]Faculty of Production Engineering, University of Bremen, Badgasteiner Str. 1, 28359 Bremen, Germany;
[6]Leibniz Institute for Materials Engineering IWT, Badgasteiner Str. 3, 28359 Bremen, Germany.

Address Correspondence to:
Sijie Lin, Ph.D. Professor
College of Environmental Science and Engineering, Tongji University
1239 Siping Road, Shanghai 200092, China
Tel: 86 21 65982325
E-mail: lin.sijie@tongji.edu.cn

Suman Pokhrel, Dr. habil
Faculty of Production Engineering, University of Bremen, Badgasteiner Str. 1, 28359 Bremen, Germany and Leibniz Institute for Materials Engineering IWT, Badgasteiner Str. 3, 28359 Bremen, Germany;
Tel: +49 42121851218
E-mail: spokhrel@iwt.uni-bremen.de

Abstract

Redox active metal oxide nanoparticles show varying oxidizing capacities and injury potentials towards biological systems. Here, two metal oxide libraries including transition metal-doped Co_3O_4 and PdO-Co_3O_4 with strong chemical contacts were design-synthesized and used to investigate their biological injury potential and mechanisms using zebrafish as a model organism. Among different dopants, Cu significantly increased the oxidizing capacity of Co_3O_4. Increased amount of PdO resulted in higher density of heterojunctions that also led to higher oxidizing capacity. The oxidizing capacity of these nanoparticles was positively correlated with higher mortality of dechorionated embryos and severe larval skin injury upon exposure. Using transgenic zebrafish *Tg*(*LysC:*eGFP), we show in real-time that the redox active nanoparticles induced skin injury and activated the infiltration of immune cells. Such inflammatory response was confirmed by the increased mRNA expression level of *Nrf2a, HO-1, IL-1β,* and *IL-6* genes. Although the exposure to the nanoparticles alone were not lethal, the skin injury did lower the tolerance level against other environmental contaminants. More importantly, after withdrawing from the nanoparticle exposure, larvae with skin injury could recover within 24 hours in uncontaminated medium, indicating such injury was transient and recoverable.

Increasing evidence suggests that the electronic band structure of semiconductor nanoparticles plays a key role in determining their toxicity in biological systems.[1-4] The overlap between the conduction band energy of metal oxide nanoparticles and the biological redox potential (-4.12 ~ -4.84 eV) leads to electron drainage from the biomolecules, disruption of cellular redox equilibrium, and oxidative stress in cells and animal lung.[1, 3] Heterojunction formation on the nanoparticle surface separates the electron hole pairs more efficiently, allowing both electrons and holes to react with surface and/or near surface oxygen and water molecules, respectively, to form oxidizing reactive oxygen species (ROS).[4] And biological injuries exerted upon exposure to these redox active nanoparticles require intimate nano-bio interactions, *i.e.* direct contact between nanoparticle and the cell membrane, bacterial cell wall or epithelial lining of animal lung.[2, 3, 5, 6]

Zebrafish frequently used for biomedical research and toxicity screening possesses unique features in helping dissect *in vivo* injury mechanisms of nanoparticles.[7-9] With the protection of chorions, zebrafish embryos have limited contact with nanoparticles through exposure by water immersion.[10, 11] As a result, only a few soluble metal oxide nanoparticles exert hatching interference due to hatching enzyme inactivation *via* metal ions, including Zn^{2+}, Ni^{2+} and Cu^{2+}.[12-14] However, recent studies showed that zebrafish larval skin became the main targeted organ of nanoparticle exposure after embryo hatching.[15, 16] And the toxic effect originated from the interplay between nanoparticle and larval skin epithelium. Nonetheless, the injury mechanism and the contributing factors of the nanoparticle characteristics remain to be further explored.

In this study, we set out to design-synthesize two metal oxide libraries of Co_3O_4-based

nanoparticles, through transition metal doping and surface heterojunction formation. The oxidizing capacity of these nanoparticles were determined by quantifying the abiotic ROS generation, followed by toxicity assessment using dechorionated embryos and larvae. The amount of abiotic ROS generation positively correlated with the increased mortality of dechorionated embryos and the extent of larval skin injuries. Besides injuries on the larval fin, it is intriguing to see that the redox active nanoparticles also targeted the hair cells, a specific type of chemo- and mechano-sensitive cells at the lateral line of the larvae. Taking advantage of a transgenic zebrafish strain *Tg*(*LysC:*eGFP) with GFP positive macrophages and neutrophils, we show in real-time the infiltration of immune cells responding to the injury. Furthermore, the skin injury exerted by redox active nanoparticles would lower the overall tolerance level of zebrafish against other known toxicants in the environment. However, the injured larvae could recover within 24 hours recuperating in clean medium after withdrawing from the nanoparticle exposure.

Results

Libraries of Co_3O_4-based Nanoparticles Synthesized by Flame Spray Pyrolysis

To obtain metal oxide nanoparticle libraries with varying redox activities, flame spray pyrolysis (FSP) was used to design-synthesize two libraries of Co_3O_4-based metal oxides, *i.e.* transition metal (Fe-, Cr-, Cu-, and Mn-) doped Co_3O_4 and PdO-Co_3O_4 with surface heterojunctions. In both cases, the basic structure of the nanoparticles, *i.e.* Co_3O_4, was preserved during aerosol flame synthesis. While doping was able to substitute Co beyond its solubility limit in the gas phase, the tight chemical contact between PdO and Co_3O_4 formed heterojunctions on the nanoparticle surface. As shown in Fig. 1a and b, the primary particle size of the as-synthesized nanoparticles demonstrated by Transmission Electron Microscopy (TEM) were within a range of 10.9 nm - 12.4 nm. The lattice spacing derived from the

magnified and Fourier transformed high resolution images for pure, 10% Fe-, Cr-, Mn- and Cu-doped Co_3O_4 were 0.244, 0.303, 0.454, 0.256 and 0.244 nm, respectively. The lattice spacing for pure (0.244 nm) and 10% Mn-doped Co_3O_4 (0.256 nm) reasonably matches with the XRD signal occurring at 36.87° 2θ (0.248, nm 1 1 3) while the parameters for 10% Fe (0.303 nm) and 10% Cu-doped Co_3O_4 (0.294 nm) match with the signal occurring at 30.71° 2θ (0.298 nm, 0 0 2). Such lattice spacing for 10% Cr-doped Co_3O_4 (0.454 nm) matches with the signal occurring at 19.02° 2θ (0.466 nm). The variations in the spacings were due to different particle orientations during TEM measurements. The representative STEM images showed that the PdO on Co_3O_4 were crystalline and chemically attached, forming the surface heterojunctions (Fig. 1b). As summarized in Table 1, the surface areas of the Co_3O_4-based nanoparticles were in the range of 73.6 to 93.3 m^2/g with equivalent particle size of 13.2 nm to 10.9 nm. While dispersed in Holtfreter's medium, the hydrodynamic diameters of these nanoparticles were from 85.0 nm to 122.8 nm with negative surface charge for all Co_3O_4-based nanoparticles.

The X-ray powder diffraction (XRD) measurements were performed to determine the crystallite size and phase compositions of these Co_3O_4-based nanoparticle libraries. The XRD patterns were Rietveld refined and the lattice parameters for cubic Co_3O_4 were extracted. Significant peak shifts were observed for different transition metal-doped Co_3O_4 (Fig. 1c). Considering the main reflection (100% intensity reflection) at 36.9° 2θ (pure Co_3O_4, d = 0.244 nm), the Fe-doped Co_3O_4 showed the largest shift of 0.65° 2θ while the other nanoparticles such as Cu-, Mn- and Cr-doped Co_3O_4 showed 0.04, 0.04, and 0.3° 2θ shift, respectively, in the XRD patterns, clearly suggesting easy Cu and Mn incorporation compared to Cr and Fe (with larger shift in the patterns). The 2θ shifts were verified by the increase in the cubic lattice distance *via* transition metal doping. The cubic lattice parameter of pure Co_3O_4 was found to

be 0.8083 nm while the parameters for Cu-doped, Mn-doped, Cr-doped and Fe-doped Co_3O_4 were 0.8095, 0.8098, 0.8121 and 0.8195 nm, respectively. Unlike transition metal-doped Co_3O_4, the XRD measurement of 1, 4 and 6% PdO-Co_3O_4 showed no peak shifts in their 2θ positions (Fig. 1c). The PdO is not incorporated in Co_3O_4 which is due to the significant differences in the ionic radii of Pd and Co. The ionic radius of Pd^{2+} (0.1 nm) is much larger than the Co^{2+} (0.074 nm) and Co^{3+} (0.072 nm) in both the tetrahedral and/or octahedral coordination making large PdO doping in small Co_3O_4 lattice difficult. The small ionic radii of Fe^{3+}, Cu^{2+} Cr^{3+}, Mn^{3+} are 0.055, 0.073, 0.0615 and 0.058 nm, respectively compared to cobalt are easily incorporated and hence doping was possible.

Electron energy loss spectroscopy (EELS) measurements were used to determine the band energy of these Co_3O_4-based nanoparticles (Fig. 1d). The Fe^{3+}, Cr^{3+}, Mn^{3+}, Cu^{2+} -edges confirm the presence of vacant 3*d*-orbitals in Co_3O_4 for charge flow. Transition metals such as Fe, Cr, Mn and Cu, lower the band energies by trap level induction.[17-19] These levels allow electron flow across the interface depending on the nature of space charge layer created due to mismatch of the charges at the interface.[4] The two absorption edges of Fe-doped Co_3O_4 at ~ 708 (L_3) and 721 (L_2) eV with 13 eV of coupling constant show characteristic signals of Fe^{3+} due to charge-transfer transition between the Fe^{3+} *d*-electrons and the conduction or valence band of Co_3O_4.[18, 20] Similarly, the two Cr-edges occurring at 575 (L_3) and 584 eV (L_2) with 8 eV is the characteristic signal for Cr^{3+}*d*-electron transition. The weak Cu-edge was observed at 931 (L_3) and 951 (L_2) eV, characteristic of Cu^{2+} *d*-electrons transition. The lower energy state of 3*d*-electrons from different dopants relative to the ground state electrons of Co_3O_4 could easily allow electron flow across the interface through the conduction band of Co_3O_4 nanoparticles. In PdO-Co_3O_4 libraries, no edges of Pd were observed besides Co, suggesting the homogeneous distribution of PdO even at lower PdO content. Based on the UV-Vis-UPS

measurements from our earlier work, the conduction band energies of 1%, 4% and 6% PdO-Co_3O_4 were found to be in the range of -4.50 to -4.52 eV (Tab. 1). These conduction band positions were well within the biological redox potential (-4.12 ~ -4.84 eV) for efficient charge transfer at the bio-nano interface consequently may induce disruption of biological redox couples.

The dissolution profiles of these particles in Holtfreter's medium were determined using ICP-MS. For each doped nanoparticle, the initial nominal concentrations were 50 ppm. As demonstrated in Fig. 1e, there was minimum to no Co dissolution from all Co_3O_4-based nanoparticles (0.11 ± 0.06 to 1.04 ± 0.33 ppm). Low metal dissolution was observed in 10% Cr-, Mn-, Fe-doped Co_3O_4 and PdO-Co_3O_4, while significant amount of Cu dissolution was observed, with 3.02 ± 0. 36 ppm dissolved from 50 ppm.

The Redox Activity of Co_3O_4-based Nanoparticles Depended on the Dopant and the Density of Surface Heterojunctions

To evaluate the redox activity of two libraries of Co_3O_4 nanoparticles, dichlorofluorescein-based fluorescence assay (DCF assay) was performed abiotically. As shown in Fig. 1f, significant increase of fluorescence intensity was observed for all transition metal doped Co_3O_4 nanoparticles with Cu-doped Co_3O_4 (most dissolvable nanoparticles) generating the highest ROS. In the PdO-Co_3O_4 library, the abiotic ROS generation correlated with the amount of PdO, indicating the density of surface heterojunctions contributing to the ROS generation (Fig. 1g). In both cases, nanosized Fe_2O_3 was used as a negative control and N-acetyl cysteine (NAC) at 400 μM was used as an ROS scavenger. The abiotic ROS generation by these Co_3O_4-based nanoparticles led to the disruption of redox couples, demonstrated by a GSH depletion assay

(Fig. S1), in which significant lowered GSH/GSSG ratios were found after treatment of the Co_3O_4-based nanoparticles, with 4% and 6% PdO-Co_3O_4 being the most significant ones.

Table 1. Physicochemical characterizations of Co_3O_4-based nanoparticles.

Co_3O_4-based nanoparticles	**Surface area (m^2/g)**	**Particle size (d_{BET}) (nm)**	**Crystallite size (d_{XRD}) (nm)**	**Conduction band energy (eV)**	**Band gap energy (eV)**	**DLS (nm)**	**Zeta potential (mV)**
Pure Co_3O_4	85.4	11.5	10.5	-4.61	2.56	85.0 ± 1.6	-8.2 ± 0.2
10% Fe-doped	93.3	10.9	10.4	-4.45	2.82	112.3 ± 5.4	-6.4 ± 0.3
10% Cr-doped	89.7	11.1	9.3	-4.49	2.73	93.2 ± 14.7	-1.0 ± 0.3
10% Mn-doped	89.6	11.2	10.5	-4.47	2.77	85.3 ± 14.9	-1.2 ± 0.6
10% Cu-doped	79.2	12.4	10.9	-4.45	2.84	119.7 ± 6.6	-13.0 ± 1.5
1% PdO-Co_3O_4	73.6	13.2	9.3	-4.50	2.78	116.1 ± 4.2	-10.5 ± 0.5
4% PdO-Co_3O_4	82.8	11.4	8.9	-4.51	2.76	122.8 ± 7.5	-9.8 ± 0.8
6% PdO-Co_3O_4	78.6	11.7	8.7	-4.52	2.74	109.7 ± 3.9	-10.4 ± 0.2

Co_3O_4-based Nanoparticles Exerted Mortality on Dechorionated Embryos and Skin Injury on Hatched Larvae

The injury potential due to redox activity of both libraries of Co_3O_4 nanoparticles was investigated using zebrafish embryos and larvae. As previously demonstrated, a direct nano-bio interaction between nanoparticle and biological entity was essential for nanotoxicity analysis. For this reason, zebrafish embryos were dechorionated before exposing to each type of Co_3O_4 nanoparticles at 5 ppm -100 ppm (Fig. S2). Embryos mortality was found to be dose- and time-dependent, with the Cu-doped Co_3O_4 and 6% PdO-Co_3O_4 being the most detrimental ones. Cu-doped Co_3O_4 nanoparticles exerted significant mortality at 25 ppm and above, and the mortality increased with the exposure time. Similar trend was observed for Mn-, Cr-, and Fe-doped Co_3O_4 nanoparticles. For PdO-Co_3O_4, the mortality was in close correlation with the amount of PdO and the density of surface heterojunction, suggesting that the mortality was due to the abiotic ROS generation (Pearson $r = 0.84$). Distinctively, when embryos were exposed to these nanoparticles with intact chorion, only Cu-doped Co_3O_4 nanoparticles exerted hatching interference due to Cu^{2+} shedding without any significant mortality (Fig. S3). These results demonstrated the protective effect of chorions and also pointed out the importance of direct nano-bio interaction.

In the case of larvae, significant amount of adsorption of nanoparticles on the larval skin was observed after 24 hours exposure. The accumulation and distribution of Co_3O_4-based nanoparticles on the larval skin was examined using SEM-EDX (Fig. 2a, using larva exposed to Cu-doped Co_3O_4 nanoparticles as an example). Nanoparticles appeared to adhere on all areas of the larval skin, with the lateral line and tail fin regions being the most distinguishable. EDX element mapping showed a high degree of overlap between the Co signal and the location of nanoparticle agglomerates. The Cu signal was much more dispersed and did not overlap with

such agglomerates, indicating Cu ion was shed from the particle structure as a result of dissolution (Fig. 2a, v).

The close encounter of redox active nanoparticles with the ability to generate abiotic ROS led to larval skin injury, as demonstrated by neutral red staining (Fig. 2b). The severity of the injury was ranked based on the numbers of neutral red-stained cells. Skin and tail fin injury were observed in Cu-doped nanoparticles at 50 ppm and above (Fig. S4). Among all Co_3O_4-based nanoparticles, Cu-doped and all PdO-Co_3O_4 nanoparticles exerted the highest extent of skin injury at and above 200 ppm, followed by Mn-, Cr-, Fe-doped, and pure Co_3O_4 nanoparticles. According to Pearson correlation analysis (Fig. S5), there was strong correlations between the abiotic ROS generation and the mortality of dechorionated embryos (Pearson $r = 0.84$, $p = 0.019$), and between the abiotic ROS generation and the extent of skin injury (Pearson $r = 0.73$, $p = 0.039$).

To further explore the consequences of skin injury and investigate the response of larvae to such environmental insult, transgenic zebrafish *Tg*(*LysC:*eGFP) with GFP-positive macrophages and neutrophils was used to visualize the movement of immune cells (Fig. 2c). At normal/unexposed condition, as shown in a control (72 hpf larva, i), GFP-positive cells were mostly located in the vasculature, with majority of them attached to the endothelial wall of blood vessels. A small number of GFP-positive cells were observed to occasionally de-attach from the endothelial wall and perform immune surveillance throughout the body (Video S1). In contrast, larvae exposed to the redox active nanoparticles showed two distinctive distribution patterns of GFP-positive cells. As shown in Fig. 2c (ii and iii), GFP-positive cells were found to concentrate at the lateral line and the tail fin region of the larvae, pointing out the specific injury sites of the larval skin. These areas were in consistent with the findings using neutral red

staining. According to the hierarchical oxidative stress response, the lowest level (Tier 1) is associated with an Nrf2-mediated antioxidant defense, among which, heme oxygenase 1 (HO-1) plays an important role in restoring the redox disequilibrium.[21] In larvae exposed to the transition metal doped-Co_3O_4 (Fig. S6a), significant increases of *Nrf2a* and *HO-1* mRNA expression were observed for 10% Cr- and Mn-doped Co_3O_4 nanoparticles compared to the control. In the case of PdO-Co_3O_4 nanoparticles, the trend of *Nrf2a* and *HO-1* mRNA expression was in consistent with the amount of PdO, indicating the presence of heterojunction led to the oxidative stress in zebrafish and induced a greater extent of tier 1 responses (Fig. S6b). Furthermore, close correlations were found between the transcription levels of *Nrf2a* and *HO-1* with the biotic ROS based on DCF fluorescence (Fig. S7 and Tab. S2). Continuous building up of oxidative stress would shift the cellular response to active pro-inflammatory responses, evidenced by the transcriptional activation of cytokines, including interleukin 6 (IL-6) and interleukin 1β (IL-1β). As illustrated in Fig. S6c, significant increase of *IL-1β* was observed in larvae exposed to pure and transition metal doped-Co_3O_4 nanoparticles, and the most pronounced relative expression level was observed in 10% Cu-doped Co_3O_4 treated group. As for PdO-Co_3O_4 nanoparticle exposed larvae (Fig. S6d), the transcription of *IL-6* and *IL-1β* genes were significantly raised in all treatments (except the *IL-1β* transcription in 6% PdO treatment).

Exposure of Co_3O_4-based Nanoparticles Led to Neuromasts Hair Cells Injury and Larval Inflammatory Responses

Zebrafish lateral line system consists of a regular array of neuromasts present on the body surface, which contain chemo- and mechano-sensory hair cells shown to be susceptible to the environment.[22] In this study, redox active Co_3O_4-based nanoparticles were found to cause recognizable injury to the neuromasts hair cells after exposure (Fig. S8), with Cu-doped Co_3O_4

being the most detrimental one (Fig. S9). Using a hair cell specific fluorescent dye, 2-(4-(dimethylamino)styryl)-N-ethylpyridinium iodide (DASPEI), larvae exposed to non-dissolvable 6% PdO-Co_3O_4 nanoparticles at 200 ppm for only 5 h showed a complete loss of neuromasts hair cells (Fig. S10). To observe the inflammatory response in lateral line neuromasts, transgenic zebrafish *Tg*(*LysC*:eGFP) with immune cells in green fluorescence were exposed to 10% Cu-doped Co_3O_4 and 6% PdO-Co_3O_4 nanoparticles and the neuromasts hair cells were stained using a red version of the hair cell specific fluorescent dye, 4-(4-(dimethylamino)styryl)-N-methylpyridinium iodide (DASPMI). As demonstrated in control group (Fig. 3a), hair cells clustered along the lateral line with a regular array. Immune cells were mostly attached to the vasculature. In comparison, all hair cell clusters were lost after exposure to 10% Cu-doped Co_3O_4 nanoparticles at 200 ppm for 1 h. And immune cells were recruited surrounding the neuromasts. Similar effects were observed in 6% PdO-Co_3O_4, demonstrated by both the epifluorescence and Confocal fluorescence images (Fig. 3a). The irregular shape of immune cells indicated that they were trying to infiltrate through the tissue boundary across the endothelial wall of blood vessel to the injury sites (Fig. 3b). To further clarify the interactions between the immune cells and hair cells, a time-lapse recording was performed to trace the migration of the immune cells for 2 h. During the observed time frame (Video S2), the immune cells showed clear active movement around the injured neuromasts hair cells at the larval skin.

Skin Injury Exerted by Redox Active Nanoparticles Lowered the Larval Tolerance against Surfactants, but was Transient and Recoverable

Zebrafish skin offers as a barrier against the external disturbance.[23, 24] Although no survival issues were observed under the exposure of nanoparticles at as high as 200 ppm; the larval skin injury might reduce its defense against other environmental insults such as surfactants. To test

this hypothesis, larvae exposed to 10% Cu-doped Co_3O_4 were subsequently exposed to sodium dodecyl sulfate (SDS) at 30 ppm. Such treatment resulted in a significant decrease of survival rate to 50% at 6 h post-exposure (hpe), which was significantly different compared to the direct exposure of SDS to healthy larvae (80%, Fig. 4a, i). No injured larvae could survive at 24 hpe, while the survival rate in SDS alone group (30 ppm) was 40% at 48 hpe. Similarly, co-exposure of nanoparticles and SDS resulted in higher mortality than treatment with only SDS (Fig. 4a, ii).

Although Co_3O_4-based nanoparticles caused neuromasts hair cells injury and inflammatory response of zebrafish larvae, hair cell regeneration was observed in clean/uncontaminated medium. After exposure to 10% Cu-doped Co_3O_4 for 2 h, the injured larvae were transferred to fresh Holtfreter's medium. Time-lapse video showed an active recruitment of immune cells along the lateral line 2 h post-recovery (Video S3). Parts of the hair cells clusters were able to regenerate 8 h post-recovery and almost all of the hair cells recovered 24 h post-recovery (Fig. 4b, ii). Such regeneration capacity was observed irrespective to the duration of the exposure.

Discussion

In this work, through deliberate tuning the redox activity of Co3O4-based nanoparticles by transition metal doping and surface heterojunction formation, we demonstrated a close connection between nanoparticles abiotic ROS generation and their biological injury potential. Both zebrafish embryos and larvae were affected by the direct exposure of nanoparticles due to their oxidizing capacity. Using transgenic zebrafish larvae *Tg*(*LysC:*eGFP), we showed in real-time the activation and recruitment of immune cells to the injury site of larval skin. Although the exposure of nanoparticles was not lethal up to 200 ppm, the skin injury did lower the overall tolerance level of the larvae towards other environmental insults. More importantly,

such injury could recover within 24 hours recuperating in clean medium. This study provided a much-balanced assessment of the nature of injury by the redox active nanoparticles towards aquatic living organisms.

Toxicity studies on nanoparticles often reasoned the toxicological outcomes due to oxidative stress and ROS generation, but with very few investigated the detailed pathways of ROS generation. Based on this study, we proposed the following three bio-chemical reaction pathways for ROS generation during the interaction between zebrafish and Co_3O_4-based nanoparticles (Fig. 5). (1) ROS generation *via* charge transfer through different oxidation states of the doped metals including Mn, Cr and Fe (Pathway 1); (2) ROS generation through charge transfer from the space charge layer to the electron sink *e.g.* PdO when the particles are in tight chemical contact (Pathway 2); and (3) metal ion release *e.g.* Cu^{2+} from Cu-doped Co_3O_4 followed by protein interactions and ROS generation (Pathway 3). Transition metals such as Fe, Cu, Cr and Mn have different band states due to their vacant *d*-orbitals. These bands allow changes in the valence states through electron transfer during charge equilibration. Our electron energy loss spectroscopy (EELS) spectra showed strong absorption resonances of L2,3-edge of transition metals exhibiting strong electronic transitions from 2*p* to unoccupied 3*d* ground states of Co_3O_4 for efficient charge flow across the interface (Fig. 1d). The charge flow within the doped metal oxides lowers the band energies due to charge equilibrium facilitating the electron flow. The electrons emerging the surface react with the near surface oxygen producing unstable superoxide radicals ($O_2^{\bullet-}$), which is further reduced by water molecules generating hydroxyl radicals ($^{\bullet}OH$) and electrons for charge balance (Fig. 5, Pathway 1).

The bio-chemical pathway 2 is based on the tight chemical contact between two oxide materials (PdO and Co_3O_4 in the present work). When the conduction band (*Ec*) of the metal oxide

overlap with the biological redox potential (-4.12 ~ -4.84 eV), the cellular oxidative stress and inflammations are induced in biological organisms.[3] Such material engineering allows electron flow and adjust *Ec*, valence band (*Ev*) and Fermi (E_f) energy *via* majority charge carriers ($h+$ in the case of *p*-type Co_3O_4) during biological redox regulation. The mismatch of the fermi energies of the PdO and Co_3O_4 in the tight chemical contact results in electron transfer from Co_3O_4 to PdO during Fermi energy alignment followed by excess holes (h^+) accumulation in the space charge layers. While the electrons flowing on the PdO surface reacts with near surface oxygen giving rise to ROS as explained earlier, the holes in the space charge layer also react with the water molecules producing ROS. The bio-chemical pathway 3 is derived from the conventional metal ion toxicity paradigm. The injury exerted by Cu-doped Co_3O_4 nanoparticles were mostly contributed by Cu^{2+} shed from the nanoparticles that caused the hair cells death in the developing larvae.[26-28] Although the toxicological outcomes in these cases were (1) severe injury in the neuromasts hair cells in larvae, and (2) significant disruption of cellular redox equilibrium triggering oxidative stress, the underlining mechanisms differ depending on the specific physicochemical characteristics of the nanoparticles.

Skin epithelium of zebrafish is considered as an analogue of animal lung.[15, 16, 29]. Upon skin injury, neutrophils are firstly recruited to the injury site to eliminate any pathogens, with macrophages following to carry out phagocytosis of tissue debris, which is known as efferocytosis.[29-32] Using fluorescent live staining and transgenic zebrafish, we were able to show such immune activation upon nanoparticles exposure by following the recruitment of immune cells in the tail fin and lateral line of zebrafish larvae (Fig. 2 and 3). The recruitment of immune cells also explained the recovery of zebrafish larvae after the withdrawal of nanoparticle exposure.

In summary, we illustrated three bio-chemical reaction pathways for ROS-mediated injury exerted by redox activity nanoparticles in zebrafish. Our results showed that redox active Co_3O_4-based nanoparticles could exert biological injuries in the forms of embryo mortality, larval skin injury and hair cell death upon direct nano-bio interactions. Although skin injury lowered the larval tolerance level towards other environmental insults, zebrafish larvae could recover within 24 hours in clean/uncontaminated medium after withdrawing from the nanoparticle exposure. This work demonstrated the possibility of applying the oxidative stress paradigm established *in vitro* to an aquatic organism zebrafish *in vivo*; and more importantly it provided a balanced assessment of the biological injury potential of redox active nanoparticles.

Materials and Methods

Synthesis and physicochemical characterization of Co3O4 based nanoparticles

Two sets of Co_3O_4-based nanoparticles (pure, 1, 4 and 6% PdO doped Co_3O_4 and 10% Fe, Cr, Mn and Cu doped Co_3O_4) were synthesized using flame aerosol technology. For PdO-Co_3O_4 nanoparticles synthesis, required amounts of liquid metalloorganic precursors, cobalt napthenate (53% in mineral sprit, 6% Co, Strem Chemicals) and palladium acetylacetonate (Strem Chemicals, 99.9 % pure) dissolved in xylene were mixed together to obtain 1, 4 and 6% of PdO in Co_3O_4 before flame combustion. For instance, 336 mg of Pd acetylacetonate was mixed in 100 mL of Co naphthenate-xylene solution (0.5 M) to obtain 4% PdO-Co_3O_4. The resulting solution after mixing was sonicated at room temperature for 2 hours prior to spray for complete dissolution of solid palladium acetylacetonate. Similarly for the synthesis of 10% transition metal (Fe, Cr, Mn and Cu) doped Co_3O_4, the required amount of iron naphthenate (40% in mineral sprit, 6% Fe, Strem Chemicals), chromium (III) 2-ethylhexanoate (70% in mineral spirit, 8% Cr, Strem Chemicals), manganese naphthenate (56% in mineral sprit, 6% Mn, Strem Chemicals) and copper naphthenate (77% in mineral sprit, 8% Cu, Strem Chemicals)

were separately dissolved in xylene followed by mixing with cobalt-xylene solution. For the synthesis of 10% Fe or Cr or Mn or Cu doped Co_3O_4, 2.72 mL of 0.5M iron-naphthenate or 4.3 mL of 0.5M chromium (III) 2-ethylhexanoate or 3.1 mL of manganese naphthenate or 4.1 mL of copper naphthenate were separately dissolved in 50 mL of 0.5M cobalt naphthenate-xylene solution. During nanoparticles production, all the precursor-solvent combinations were delivered to the spray nozzle using a syringe pump at the rate of 5mL/min for combustion. The solutions were atomized using a pre-mixed gas (CH_4+O_2) flowing at the rate of 1.5+3.2 L/min with the constant pressure drop of 1.5 bar providing sufficient energy for the liquid feed combustion. The particles were formed *via* nucleation, surface growth, coagulation and coalescence in the high temperature flame environment.[33, 34] The particles were collected from the 257 mm glass filter placed in the flame reactor at a distance of 60 cm above the flame.

BET, XRD and TEM analysis

For the BET measurements, the pre-weighted nanoparticles were placed in a test bulb and placed in the vacuum degassing stations for 2 hours at 200°C before adsorption measurements in a Quantachrome NOVA 4000e gas sorption system. Data were acquired *via* adsorption/desorption cycles of a known volume of adsorbent in or out of a sample cell maintained at 77 K. The PdO-Co_3O_4 and transition metal (Fe, Cr, Mn and Cu) doped Co_3O_4 nanoparticles were pressed on the single crystalline 16 mm diameter Si-holders followed by loading in D8 Advance diffractometer. The instrument is equipped with a primary Johansson monochromator producing Cu-$K_{\alpha 1}$ (λ = 0.15406 nm) radiation with fixed divergence of 0.4° provided with primary and secondary 2.5° aperture Soller slit. A continuous scan in the range of 3-90° 2θ and an integration step width of 0.0118613° 2θ was obtained using a slit of 0.2 mm in the position of the primary focus and a LynxEye sensitive detector with 3° total aperture and 0.015625° channel width. The crystallite size and phase compositions were determined

from the Rietveld refinements of the XRD patterns of the nanoparticles using the BRASS program.[35, 36] The refined parameters included scale factors, lattice parameters, crystallite size and microstrain parameters. The structural models used were: Co_3O_4 (ICSD collection code 36256) with cubic cell and space group $Fd\bar{3}m$, PdO (ICSD collection code 41617) with tetragonal space group I4/mmm. The quality of the refinement was evaluated based on R factors, *i.e*. R_{wp}, R_{Bragg} and the background corrected R'_p. The instrumental contribution to the peak broadening was taken into account during the full profile fitting by instrumental parameters derived from a fit of standard crystalline LaB_6. The low resolution TEM, the corresponding selected area electron diffractions (SAED), and high-resolution microscopic imaging (HRTEM) of the specimens was imaged using a FEI Titan 80/300 microscope equipped with a Cs corrector for the objective lens. The EDX detector was used for the elemental quantification. A Fischione high angle annular dark field detector (HAADF), GATAN post-column imaging filter and a cold field emission gun operated at 300kV as an acceleration voltage was used.

Hydrodynamic diameters and zeta potential were obtained using a ZetaSizer Nano instrument (ZS 90, Malvern Instruments Ltd., UK) dispersed with Holtfreter's medium at a concentration of 10 ppm. Dissolution characteristics of nanoparticles was determined by inductively coupled plasma mass spectroscopy (ICP-MS, Agilent 7700). All the eight Co_3O_4-based nanoparticles were suspended in Holtfreter's medium at 50 ppm nominal concentration and kept at 28.5 ℃ for 48 h. Supernatants were collected by centrifugation at 9600 *g* for 40 min. After digestion with nitric acid, the concentration of each corresponding metal ions were quantified by ICP-MS. The total dissolved metal concentration for each Co_3O_4-based nanoparticle was calculated.

Zebrafish husbandry and maintenance

The AB wild-type and transgenic strain *Tg*(*LysC:*eGFP) adult zebrafish (*Danio rerio*) were maintained at 28 ± 0.5 ℃ on a 14 h:10 h light/dark cycle in a fish breeding circulatory system (Haisheng, Shanghai, China). Two pairs of male/female fish were placed in a single mating tank with a divider one day prior to spawning. Spawning was triggered by removing the divider in the morning. Embryos were collected after 2 hours, washed with 0.5 ppm methylene blue solution, and then transferred to Holtfreter's medium in a petri-dish. Healthy and fertilized embryos at the same developmental stages were selected for further experiments under a stereomicroscope (Olympus-SZ61, Olympus Ltd., Japan). All procedures were carried out in accordance with the Animal Ethics Committee at Tongji University (Protocol #TJLAC-018-020).

Assessment of abiotic total reactive oxygen species generation (ROS) and GSH depletion

A fluorescent dye 2',7'-Dichlorodihydrofluorescein diacetate (H_2DCFDA) was used to determine the total abiotic ROS generation by Co_3O_4-based nanoparticles. A freshly prepared stock solution of 1.0 mM H_2DCFDA was used for all experiments. The acetate group of H_2DCFDA was cleaved by 0.1 M sodium hydroxide (NaOH) solution at room temperature for 30 min before mixing with Co_3O_4-based nanoparticles to assess the abiotic ROS generation. The nominal 10 μM concentration of H_2DCFDA and 100 ppm of Co_3O_4-based nanoparticles used were used. After incubation at 28 ℃ in dark for 60 min, the mixture was centrifuged at 9600 *g* for 5 min followed by transferring 200 μL of the supernatant to a 96-well plate (Thermo Fisher Scientific 265301, US) for fluorescence measurements (Varioskan ™ LUX, Thermo Fisher Scientific, US). DCF fluorescence intensity was collected centered at 530 nm excited by 485 nm to determine the level of abiotic ROS generation. N-acetyl-L-cysteine (NAC, 400 μM) were used as ROS scavenger. 1% hydrogen peroxide (H_2O_2) was used as the positive control. The GSH concentration was determined by a commercially available kit as described

previously.

Toxicity assessment of Co3O4-based nanoparticles using zebrafish embryos

The detached chorions of zebrafish embryo at 4 hpf were digested with 20 mg/mL pronase (Sigma, US) in a glass beaker. The digestion process was examined under a stereomicroscope. Holtfreter's medium was added immediately when the first dissociation of chorion was observed. The dechorionated embryos were then transferred to 96-well plate with 100 μL of Co_3O_4-based nanoparticle suspensions at 5 ppm - 100 ppm nominal concentrations for toxicity assessment. Three replicates were carried out for each treatment, each containing 12 embryos, thus 36 embryos for each treatment for statistical analysis. Toxicity endpoints, such as abnormal phenotype, and mortality rate were assessed at 24, 48 and 72 hpf using a bright field stereomicroscope (Olympus-SZ61, Olympus Ltd., Japan). The surviving developing larvae at 72 hpf were collected for biotic ROS assessment and RNA extraction. The fluorescence values labeled by H_2DCFDA were used to determine the biotic ROS generation. The average of 29 multiple points was used for one well fluorescence value through optic bottom reading on a microplate reader (Varioskan ™ LUX, Thermo Fisher Scientific, US). Samples for RNA extraction were frozen at -80 °C until processing.

Microinjections were performed with 20 psi injection pressure on a pneumatic microinjection system (PV830 Pneumatic Picopump, WPI). A mixture of H_2DCFDA and 10% Cu-doped Co_3O_4 nanoparticles were co-injected into embryos chorionic sac at 1 hpf. The concentration of H_2DCFDA and Cu-doped Co_3O_4 nanoparticles used were 10 μM and 100 ppm, respectively. N-acetyl-L-cysteine (NAC, 100 μM) were co-injected as ROS scavenger. The biotic ROS generation was assessed at 1, 24, 48 and 72 hpf, determined by the fluorescence intensity of DCF centered at 530 nm excited by 485 nm using a microplate reader (Varioskan ™ LUX,

Thermo Fisher Scientific, US). The average fluorescence value of 29 multiple points was presented and all the data was normalized to control before statistical analysis. The mortality rate was assessed at each testing point accordingly.

Skin injury assessment in zebrafish larvae

Scanning electron microscope (SEM, Hitachi S4800, Japan) was used to investigate the accumulation and distribution of 10% Cu-doped Co_3O_4 nanoparticles in the zebrafish larval skin. An Energy Dispersive X-ray (EDX) spectrometer microanalysis system (Oxford Instrument, X-Max 50 mm^2, Horiba, Japan) coupled with SEM was used for the elemental composition analysis. Specifically, zebrafish developing larvae (72 hpf) were exposed to 10% Cu-doped Co_3O_4 nanoparticles at 200 ppm for 24 h. After that, zebrafish larvae were collected and incubated with 4% paraformaldehyde (Leagene Biotechnology Co., Ltd., Beijing, China) for 4 h. Gradient concentration of ethanol at 25%, 50%, 75%, 95% and 100% were used for the dehydration. Each step lasted for 20 min. Samples were then mounted on the carbon tape to completely dry, and sputtered with gold before loading on the SEM-EDX for analysis. The extent of skin injury on developing larvae (72 hpf) exerted by Co_3O_4-based nanoparticles was assessed using a eurhodin dye such as Neutral Red (NR). *Tg*(*LysC:*eGFP) transgenic zebrafish larvae were used for the observation of immune cells migration. Specifically, after exposure to 10% Cu-doped and 6% PdO-Co_3O_4 nanoparticles at 200 ppm for 2 h, transgenic zebrafish developing larvae at 72hpf were anaesthetized in 0.01% tricaine solution, and embedded in 1% low-melt agarose for imaging positioning. Fluorescence images with FITC filter set (Ex: 488 nm, Em: 540 nm) were captured using a fluorescence microscope (Olympus-SZ2-ILA, Olympus Ltd., Japan).

Sequential and co-exposure of nanoparticles with surfactant towards zebrafish larvae

The anionic surfactant, sodium dodecyl sulfate (SDS) was used to observe the combined effect with nanoparticles on zebrafish larvae. Two different exposure scenarios were conducted, i.e., sequential and co-exposure. 10% Cu-doped Co_3O_4 at 200 ppm and SDS at 25 and 30 ppm were used respectively. For sequential exposure, zebrafish larvae (72 hpf) were exposed to nanoparticles for 5 h first, then washed by fresh Holtfreter's medium, and transferred to SDS solutions in 96-well plates. Healthy larvae without any pre-treatment were exposed to SDS as the control. For co-exposure, healthy larvae were transferred to 96-well pates with 200 ppm nanoparticles and SDS at two different concentrations. Healthy larvae exposed to nanoparticles alone, SDS alone and Holtfreter's medium were investigated at the same time. Three replicates were carried out for each treatment, each contains 12 larvae, thus 36 larvae for each treatment for statistical analysis. The survival percentage of each treatment was counted every two hours until 48 h.

Inflammatory response assessment in zebrafish neuromasts hair cells

A neuromasts hair cells specific dye, 2-(4-(dimethylamino)styryl)-N-ethylpyridinium iodide (DASPEI, ATT Bioquest) were used to determine the hair cells injury in zebrafish larvae. After exposure in Co_3O_4-based nanoparticles at 200 ppm for 2 h, zebrafish larvae were rinsed three times with Holtfreter's medium, and incubated with 50 μgmL^{-1} of DASPEI for 15 min. Labeled larvae were rinsed with Holtfreter's medium, anaesthetized and positioned for observation under a fluorescence microscope (Olympus-SZ2-ILA, Olympus Ltd., Japan). Fluorescence images were captured with FITC filter set (Ex: 488 nm, Em: 540 nm). Regeneration ability of hair cells were assessed by transferring the zebrafish larvae back to fresh Holtfreter's medium after exposure to 10% Cu-doped Co_3O_4 nanoparticles for different hours (1 h, 2 h, 3 h, 4 h and 5 h). The larvae were stained and observed under the fluorescence microscope every two hours to investigate the regeneration ability of neuromasts hair cells.

Tg(*LysC:*eGFP) transgenic zebrafish larvae and another hair cell red dye, 4-(4-(dimethylamino)styryl)-N-methylpyridinium iodide (DASPMI, Molecular Probes), were introduced for the observation of immune cells migration. 10% Cu-doped and 6% PdO-Co_3O_4 nanoparticles were selected as examples to represent these two Co_3O_4-based nanoparticles libraries. After exposure at 200 ppm for 1 h, 2 h, 3 h, 4 h and 5 h, zebrafish larvae were rinsed three times with Holtfreter's medium and incubated with 50 μgmL^{-1} of DASPMI for 15 min. Same process, *i.e.* rinsing, anesthesia and positioning were performed on fluorescence labeled larvae. Fluorescence images were captured with FITC filter set (Ex: 488 nm, Em: 540 nm) and Texas Red filter set (Ex: 540 nm, Em: 620 nm) under a fluorescence microscope (Olympus-SZ2-ILA, Olympus Ltd., Japan). Two fluorescent channel images were merged using ImageJ (Fiji Is Just ImageJ). Confocal Laser Scanning Microscope (FV3000, Olympus Ltd., Japan) was used to observe the interactions between the immune cells and hair cells. Time-lapse action was performed with the settings of one image per min and the total time as 2 h, thus 120 pictures in total to capture the immune cells migration.

Real time RT-qPCR assay

RNA was extracted using a commercial total RNA extraction kit (Omega Bio-tek, Inc., Norcross, GA, US). RNA concentration was quantified by NanoDrop 2000 spectrophotometer (Thermo Fisher Scientific, US). Total RNA (500 ng) was reverse transcribed using the RevertAid First Strand cDNA Synthesis Kit (Thermo Fisher Scientific, US) following the manufacturer's protocol. cDNA samples were stored at -20 °C prior to RT-qPCR. Transcription of target genes was quantified by relative RT-qPCR using an Applied Biosystems® 7500 Real-Time PCR System (Applied Biosystems, Inc., Waltham, MA, US). Reaction mixtures were formulated using Absolute qPCR SYBR Green Mix (Thermo

Scientific). Thermal cycling conditions were: 95 °C for 3 min, 35 cycles of 3-step amplification of 30 s at 95 °C, 30 s at 57 °C and 30 s at 72 °C. Primer sequences are listed in Table S1. The transcription level of each target gene was normalized to zebrafish *β-action* and then calculated relative to control using the $2^{-\Delta\Delta Ct}$ method. All qPCR reactions were conducted in triplicate on each sample.

Statistical analysis

All treatments were performed with at least three replicates. Data were reported as average ± standard deviations (SD). Student's T-test was used to evaluate the statistically significant differences of the ROS production, survival rates, relative mRNA expression levels between the treatment groups and the negative control group; the biotic ROS production and mortality rates between the 10% Cu-doped Co_3O_4 nanoparticles group and the group with the introduction of NAC in microinjection assay. One-way analysis of variance (ANOVA) was conducted to test the statistical differences between the abiotic ROS generation in two Co_3O_4-based nanoparticles libraries compared to the pure Co_3O_4 nanoparticles. Tukey's post hoc tests were used to determine differences among means in ANOVA tests generating significant results. Person correlation analysis were performed between the abiotic ROS and biological injuries in zebrafish, *i.e.* mortality rate and skin injured level, ROS and mortality of embryos in microinjection assay, and biotic ROS and mRNA transcription levels. Statistically significant differences were considered when p values were lower than 0.05.

Figure legends

Fig. 1 Physicochemical characterizations and redox activity of Co_3O_4-based nanoparticles. **a** Representative TEM micrographs of transition metal-doped Co_3O_4 nanoparticles (up); Magnified TEM micrographs of transition metal-doped Co_3O_4 nanoparticles (middle); Lattice distances derived from magnified and Fourier transformed high resolution images (bottom). **b** STEM investigation of 4 and 6% PdO-Co_3O_4 nanoparticles show the formation of surface heterojunction between the single-crystalline PdO particle, orientated in the (0 0 2) direction, and a single-crystalline Co_3O_4 particle, orientated in the (1 1 3) direction. **c** XRD analysis of Co_3O_4-based nanoparticles. Different transition metal-doped resulted in significant peak shifts of Co_3O_4 and such peak shift were absent in PdO-Co_3O_4 nanoparticles. **d** EELS analysis to determine the band energy of Co_3O_4-based nanoparticles. The transition metals Fe^{3+}, Cr^{3+}, Mn^{3+}, and Cu^{2+} -edges confirm the presence of vacant 3*d*-orbitals in Co_3O_4 for charge flow. **e** Dissolution characteristics of Co_3O_4-based nanoparticles in Holtfreter's medium determined by ICP-MS. Minimum amount of Co dissolution were observed in all Co_3O_4-based nanoparticles (0.11 ± 0.06 to 1.04 ± 0.33 ppm). While significant amount of Cu dissolution was observed (3.02 ± 0. 36 ppm) in 48 hours as a result of Cu doping. **f** Pure and transition metal-doped Co_3O_4 nanoparticles generated recognizable amounts of abiotic ROS based on the fluorescence intensity measurement. Among them, Cu-doped Co_3O_4 generated the highest ROS. The presence of NAC at 400 μM was able to sequester the abiotic ROS except for Cu-doped Co_3O_4. **g** PdO-Co_3O_4 nanoparticles significantly enhanced DCF fluorescence compared to pure Co_3O_4, suggesting surface heterojunctions led to increased ROS generation.

Fig. 2 Skin injury assessment of Co_3O_4-based nanoparticles in zebrafish larvae. **a** SEM-EDX images showed the adsorption and distribution of Co_3O_4-based nanoparticles on the larval skin

and tail fin region (larvae exposed to Cu-doped Co_3O_4 (i-iv) as representative); EDX element mapping showed a high degree of overlap between the Co signal and the nanoparticle agglomerates. The Cu signal was highly dispersed and did not overlap with the agglomerates, suggesting the Cu ion dissolution (v). **b** The extent of skin injury on zebrafish larvae exerted by Co_3O_4-based nanoparticles was assessed using a eurhodin dye, Neutral Red (NR). The injured cells on the larval skin were stained in red. The injury level was ranked based on the number of stained cells are presented in the table. **c** Use of transgenic zebrafish *Tg*(*LysC:*eGFP) with GFP-positive macrophages and neutrophils to visualize the movement of immune cells. Two of the most detrimental Co_3O_4 nanoparticles, *i.e.* 10% Cu-doped Co_3O_4 and 6% PdO-Co_3O_4, were used to expose to the transgenic larvae. (i) In a control larva, GFP-positive cells were mostly located in the vasculature, with majority of them attached to the endothelial wall of blood vessels. (ii) Cu-doped Co_3O_4 exposure resulted in the migration of immune cells to the lateral line (indicated by red arrows). (iii) PdO-Co_3O_4 exposure led to the migration of immune cells to the tail fin region. (iv) Magnified fluorescent image showed the infiltration of GFP-positive cells to the tail fin.

Fig. 3 Inflammatory responses of zebrafish larvae after exposure to Co_3O_4-based nanoparticles. **a** Use of DASPMI (4-Di-1-ASP) to stain the hair cells on 6 dpf *Tg*(*LysC:*eGFP) zebrafish larvae. Hair cells cluster were lost and the migration of immune cells to the larval neuromasts was observed after 1 h exposure of 10% Cu-doped Co_3O_4 and 6% PdO-Co_3O_4 nanoparticles at 200 ppm, respectively. Images were captured by both epifluorescence and Confocal fluorescence microscopes. **b** Magnified Confocal images of *Tg*(*LysC:*eGFP) zebrafish larvae after Cu-doped Co_3O_4 and 6% PdO-Co_3O_4 exposure. The irregular shape of immune cells indicated that they were squeezing through the tissue boundary across the endothelial wall of blood vessel to the injury sites (white arrows).

Fig. 4 Skin injury lowered the larval tolerance against surfactants, but was recoverable. **a** Sequential and co-exposure of 10% Cu-doped Co_3O_4 with SDS towards zebrafish larvae. (i) Sequential exposure: zebrafish larvae exposed to 10% Cu-doped Co_3O_4 at 200 ppm for 5 h were sequentially exposed to SDS at the concentration of 25 and 30 ppm. The sequential exposure of SDS at 30 ppm resulted in a significant decrease of survival rate to 50% at 6 hpe, compared to the direct exposure in SDS of healthy larvae (80%). No injured larvae could survive at 24 hpe, while the survival rate in SDS alone group was about 40%. (ii) Co-exposure: healthy larvae were exposed to solution with 10% Cu-doped Co_3O_4 at 200 ppm and SDS at the concentration of 25 and 30 ppm respectively. The survival rate of co-exposure treatment at 30 ppm decreased to 0% at 48 hpe. Similar result was found at the lower concentration of SDS (25 ppm). **b** Hair cells recovery after injury exerted by nanoparticles. (i) Exposure in Cu-doped Co_3O_4 at 200 ppm for 2 h resulted in a complete wipe out of neuromasts hair cells. (ii) Recovery timeline of hair cells in fresh Holtfreter's medium after exposure to Cu-doped Co_3O_4 for 2 h. Parts of the hair cells clusters were able to regenerate 8 h post-recovery (hpr) and all of the hair cells recovered 24 h post-recovery. (iii) Zebrafish neuromasts hair cells could recover after 24 h recuperating in fresh Holtfreter's medium even after 5 h post-exposure (hpe) in Cu-doped Co_3O_4 nanoparticles at 200 ppm.

Fig. 5 Possible injury pathways in relation to the physicochemical characteristics of Co_3O_4-based nanoparticles. Pathway 1: Electron equilibrium in the transition metal doped Co_3O_4 nanoparticles led to ROS generation and subsequent skin injury of zebrafish larvae; Pathway 2: Electron equilibrium in the in the tight chemical contact between Co_3O_4 and PdO led to ROS generation and subsequent injury; Pathway 3: Cu^{2+} dissolution from the Cu-doped Co_3O_4 caused hatching interference and hair cell death. Pathway 3 was adapted from the reference

25.[25]

Acknowledgement

This work was supported by NSFC Grant #21607115, #21777116, and the Fundamental Research Funds for the Central Universities awarded to S. Lin. G. Peng acknowledged the support from China postdoctoral science foundation #2018M632166.

Competing interests

The authors declare no competing financial interests.

Reference

1. Burello, E., Worth, A. P. A theoretical framework for predicting the oxidative stress potential of oxide nanoparticles. *Nanotoxicology* **5**, 228-235 (2011).
2. Kaweeteerawat, C., Ivask, A., Liu, R., Zhang, H., Chang, C. H.*, et al.* Toxicity of metal oxide nanoparticles in Escherichia coli correlates with conduction band and hydration energies. *Environ. Sci. Technol.* **49**, 1105-1112 (2015).
3. Zhang, H., Ji, Z., Xia, T., Meng, H., Lowkam, C.*, et al.* Use of metal oxide nanoparticle band gap to develop a predictive paradigm for oxidative stress and acute pulmonary inflammation. *ACS Nano* **6**, 4349-4368 (2012).
4. Zhang, H., Pokhrel, S., Ji, Z., Meng, H., Wang, X.*, et al.* PdO doping tunes band-gap energy levels as well as oxidative stress responses to a Co_3O_4 *p*-type semiconductor in cells and the lung. *J. Am. Chem. Soc.* **136**, 6406-6420 (2014).
5. Nel, A. E., MaDler, L., Velegol, D., Xia, T., Hoek, E. M. V.*, et al.* Understanding bio-physicochemical interactions at the nano-bio interface. *Nat. Mater.* **8**, 543-557 (2009).
6. Nel, A., Xia, T., Mädler, L., Li, N. Toxic potential of materials at the nanolevel. *Science* **311**, 622-627 (2006).
7. Lin, S., Zhao, Y., Nel, A. E., Lin, S. Zebrafish: An *in vivo* model for nano EHS studies. *Small* **9**, 1608-1618 (2013).
8. Bowman, T. V., Zon, L. I. Swimming into the future of drug discovery: *In vivo* chemical screens in zebrafish. *ACS Chem. Biol.* **5**, 159-161 (2010).
9. Lie, J. P., Federico, F., Lasse, E., Gareth, G., Gerbrand, K. Optical micromanipulation of nanoparticles and cells inside living zebrafish. *Nat. Commun.* **7**, 10974 (2016).
10. Hart, N. H., Donovan, M. Fine structure of the chorion and site of sperm entry in the

egg of brachydanio. *J. Exp. Zool., Part A* **227**, 277-296 (1983).

11. Bohme, S., Baccaro, M., Schmidt, M., Potthoff, A., Staerk, H. J.*, et al.* Metal uptake and distribution in the zebrafish (*Danio rerio*) embryo: Differences between nanoparticles and metal ions. *Environ. Sci.: Nano* **4**, 985-1200 (2017).
12. Lin, S., Zhao, Y., Xia, T., Meng, H., Ji, Z.*, et al.* High content screening in zebrafish speeds up hazard ranking of transition metal oxide nanoparticles. *ACS Nano* **5**, 7284-7295 (2011).
13. Lin, S., Zhao, Y., Ji, Z., Ear, J., Chang, C. H.*, et al.* Zebrafish high-throughput screening to study the impact of dissolvable metal oxide nanoparticles on the hatching enzyme, ZHE1. *Small* **9**, 1776-1785 (2013).
14. Lee, K. J., Nallathamby, P. D., Browning, L. M., Osgood, C. J., Xu, X. H. N. *In vivo* imaging of transport and biocompatibility of single silver nanoparticles in early development of zebrafish embryos. *ACS Nano* **1**, 133-143 (2007).
15. Mcleish, J. A., Chico, T. J., Taylor, H. B., Tucker, C., Donaldson, K.*, et al.* Skin exposure to micro- and nano-particles can cause haemostasis in zebrafish larvae. *Thromb. Haemostasis* **103**, 797-807 (2010).
16. Peng, G., He, Y., Zhao, M., Yu, T., Qin, Y.*, et al.* Differential effects of metal oxide nanoparticles on zebrafish embryos and developing larvae. *Environ. Sci.: Nano* **5**, 1200-1207 (2018).
17. George, S., Pokhrel, S., Ji, Z., Henderson, B. L., Xia, T.*, et al.* Role of fe doping in tuning the band gap of TiO_2 for the photo-oxidation-induced cytotoxicity paradigm. *J. Am. Chem. Soc.* **133**, 11270-11278 (2011).
18. Xiao, J., Agnieszka, K., Suman, P., Marco, S., Satyam, P.*, et al.* Doped nanoparticles: Evidence for Fe^{2+} in wurtzite coordination: Iron doping stabilizes ZnO nanoparticles *Small* **7**, 2878-2878 (2011).
19. Lakehal, A., Benrabah, B., Bouaza, A., Dalache, C., Hadj, B. Tuning of the physical properties by various transition metal doping in Co_3O_4: TM (TM = Ni, Mn, Cu) thin films: A comparative study. *Chin. J. Phys.* **56**, 1845-1852 (2018).
20. Xiao, J., Kuc, A., Pokhrel, S., Mädler, L., Pöttgen, R.*, et al.* Fe-doped ZnO nanoparticles: The oxidation number and local charge on iron, studied by 57Fe mößbauer spectroscopy and DFT calculations. *Chem. - Eur. J.* **19**, 3253-3253 (2013).
21. Meng, H., Xia, T., George, S., Nel, A. E. A predictive toxicological paradigm for the safety assessment of nanomaterials. *ACS Nano* **3**, 1620-1627 (2009).
22. Chou, S. W., Chen, Z., Zhu, S., Davis, R. W., Hu, J.*, et al.* A molecular basis for

water motion detection by the mechanosensory lateral line of zebrafish. *Nat. Commun.* **8**, 2234 (2017).

23. Le, G. D., Morvan-Dubois, G., Sire, J. Y. Skin development in bony fish with particular emphasis on collagen deposition in the dermis of the zebrafish (*Danio rerio*). *Int. J. Dev. Biol.* **48**, 217-231 (2003).
24. Liu, X., Wu, H., Liu, Q., Wang, Q., Xiao, J.*, et al.* Skin-injured zebrafish, *Danio rerio*, are more susceptible to *vibrio anguillarum* infection. *J. World Aquacult. Soc.* **46**, 301-310 (2015).
25. Pokhrel, S., Nel, A. E., Mädler, L. Custom-designed nanomaterial libraries for testing metal oxide toxicity. *Acc. Chem. Res.* **46**, 632-641 (2013).
26. Hernández, P. P., Moreno, V., Olivari, F. A., Allende, M. L. Sub-lethal concentrations of waterborne copper are toxic to lateral line neuromasts in zebrafish (*Danio rerio*). *Hear. Res.* **213**, 1-10 (2006).
27. Olivari, F. A., Hernández, P. P., Allende, M. L. Acute copper exposure induces oxidative stress and cell death in lateral line hair cells of zebrafish larvae. *Brain Res.* **1244**, 1-12 (2009).
28. Brun, N. R., Koch, B. E. V., Varela, M., Peijnenburg, W., Spaink, H.*, et al.* Nanoparticles induce dermal and intestinal innate immune system responses in zebrafish embryos. *Environ. Sci.: Nano* **5**, 904-916 (2018).
29. Mathias, J. R., Dodd, M. E., Walters, K. B., Yoo, S. K., Ranheim, E. A.*, et al.* Characterization of zebrafish larval inflammatory macrophages. *Dev. Comp. Immunol.* **33**, 1212-1217 (2009).
30. Papayannopoulos, V., Zychlinsky, A. Nets: A new strategy for using old weapons. *Trends Immunol.* **30**, 513-521 (2009).
31. Amulic, B., Cazalet, C., Hayes, G. L., Metzler, K. D., Zychlinsky, A. Neutrophil function: From mechanisms to disease. *Annu. Rev. Immunol.* **30**, 459-489 (2012).
32. Martin, C. J., Peters, K. N., Behar, S. M. Macrophages clean up: Efferocytosis and microbial control. *Curr. Opin. Microbiol.* **17**, 17-23 (2014).
33. Aruoja, V., Pokhrel, S., Sihtmäe, M., Mortimer, M., Mädler, L.*, et al.* Toxicity of 12 metal-based nanoparticles to algae, bacteria and protozoa. *Environ. Sci.: Nano* **2**, 630-644 (2015).
34. Wang, Z., Pokhrel, S., Chen, M., Hunger, M., Mädler, L.*, et al.* Palladium-doped silica-alumina catalysts obtained from double-flame FSP for chemoselective hydrogenation of the model aromatic ketone acetophenone. *J. Catal.* **302**, 10-19

(2013).

35. Pokhrel, S., Birkenstock, J., Schowalter, M., Rosenauer, A., Mädler, L. Growth of ultrafine single crystalline WO_3 nanoparticles using flame spray pyrolysis. *Cryst. Growth Des.* **10**, 632-639 (2010).

36. Pokhrel, S., Birkenstock, J., Dianat, A., Zimmermann, J., Schowalter, M.*, et al. In situ* high temperature X-ray diffraction, transmission electron microscopy and theoretical modeling for the formation of WO_3 crystallites. *Crystengcomm* **17**, 6985-6998 (2015).

Figure 1a

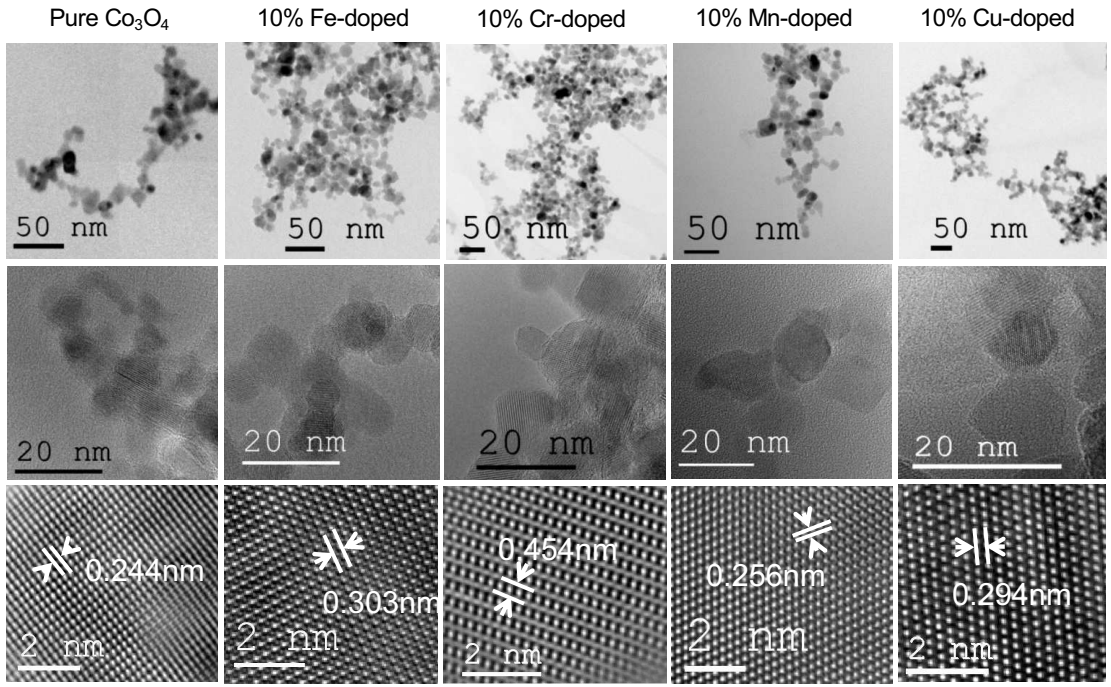
Pure Co_3O_4
10% Fe-doped
10% Cr-doped
10% Mn-doped
10% Cu-doped
50 nm
20 nm
0.244nm
0.303nm
0.454nm
0.256nm
0.294nm
2 nm

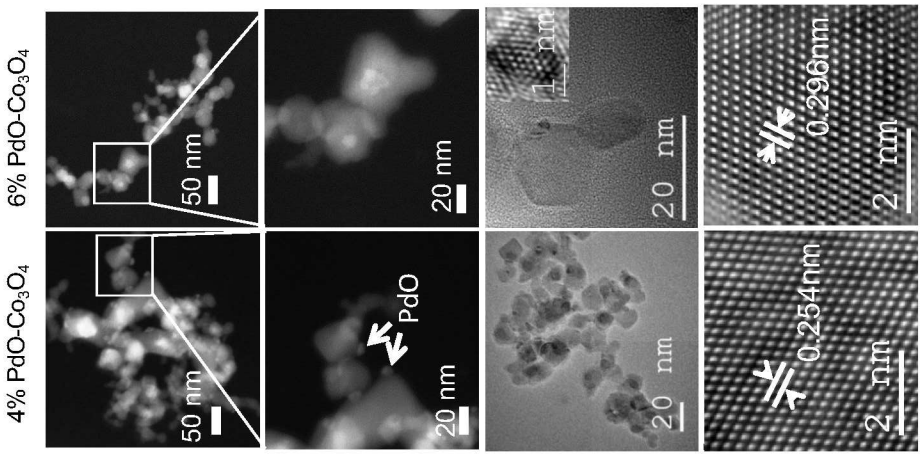
4% PdO-Co3O4
6% PdO-Co3O4
50 nm
50 nm
20 nm
20 nm
PdO
20 nm
1 nm
20 nm
0.254nm
2 nm
0.296nm
2 nm

Figure 1b

Figure 1c

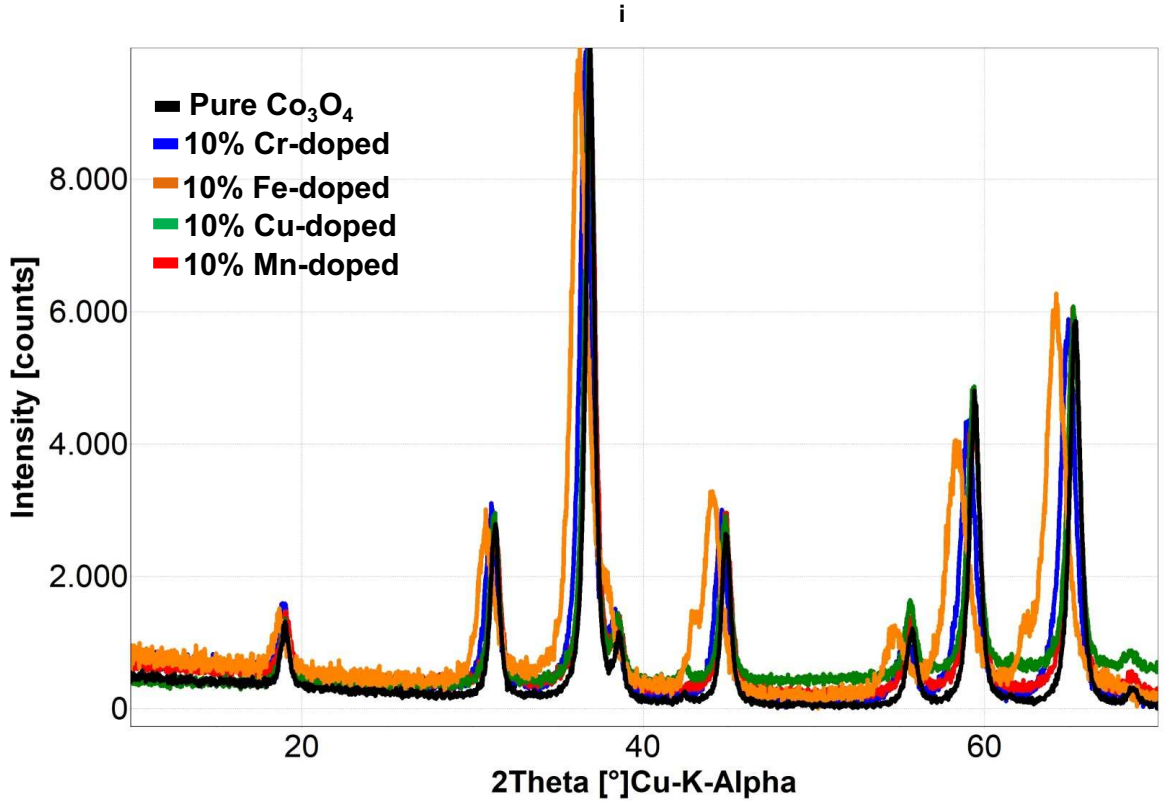
i
Pure Co_3O_4
10% Cr-doped
10% Fe-doped
10% Cu-doped
10% Mn-doped
Intensity [counts]
8.000
6.000
4.000
2.000
0
20
40
60
2Theta [°]Cu-K-Alpha

Figure 1c

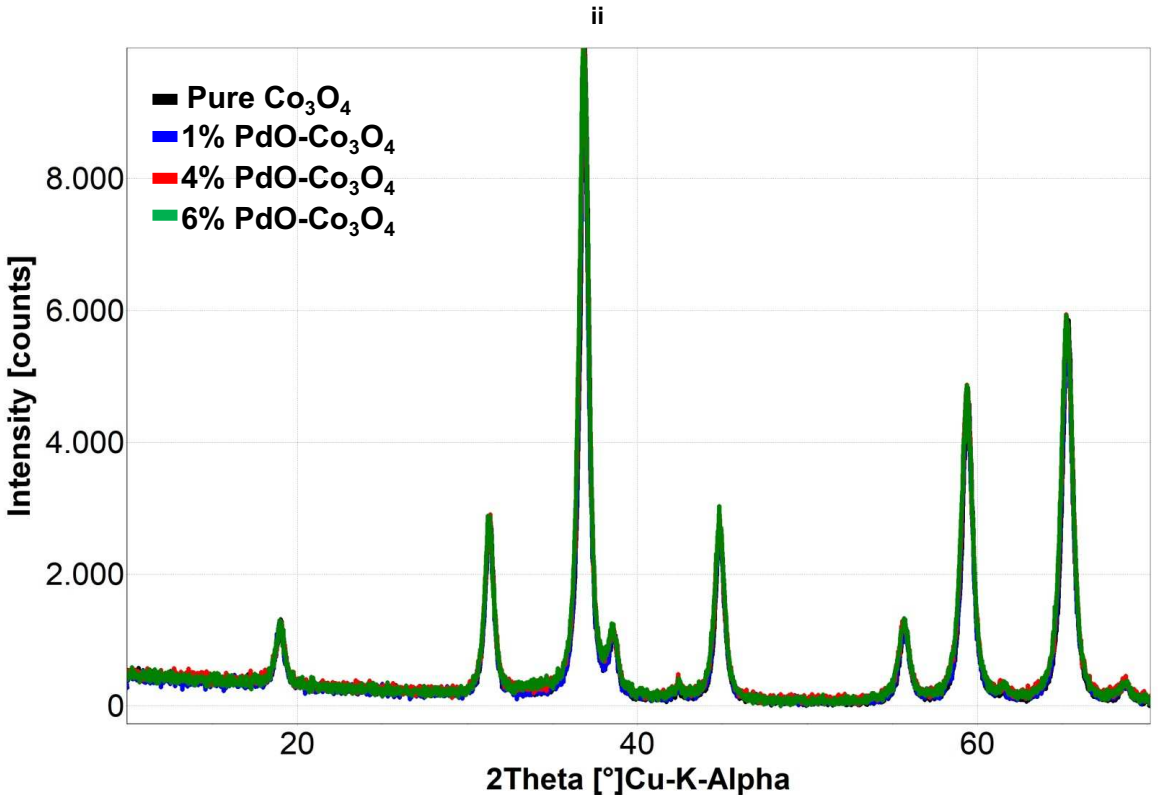
ii
Pure Co_3O_4
1% PdO-Co_3O_4
4% PdO-Co_3O_4
6% PdO-Co_3O_4
Intensity [counts]
8.000
6.000
4.000
2.000
0
20
40
60
2Theta [°]Cu-K-Alpha

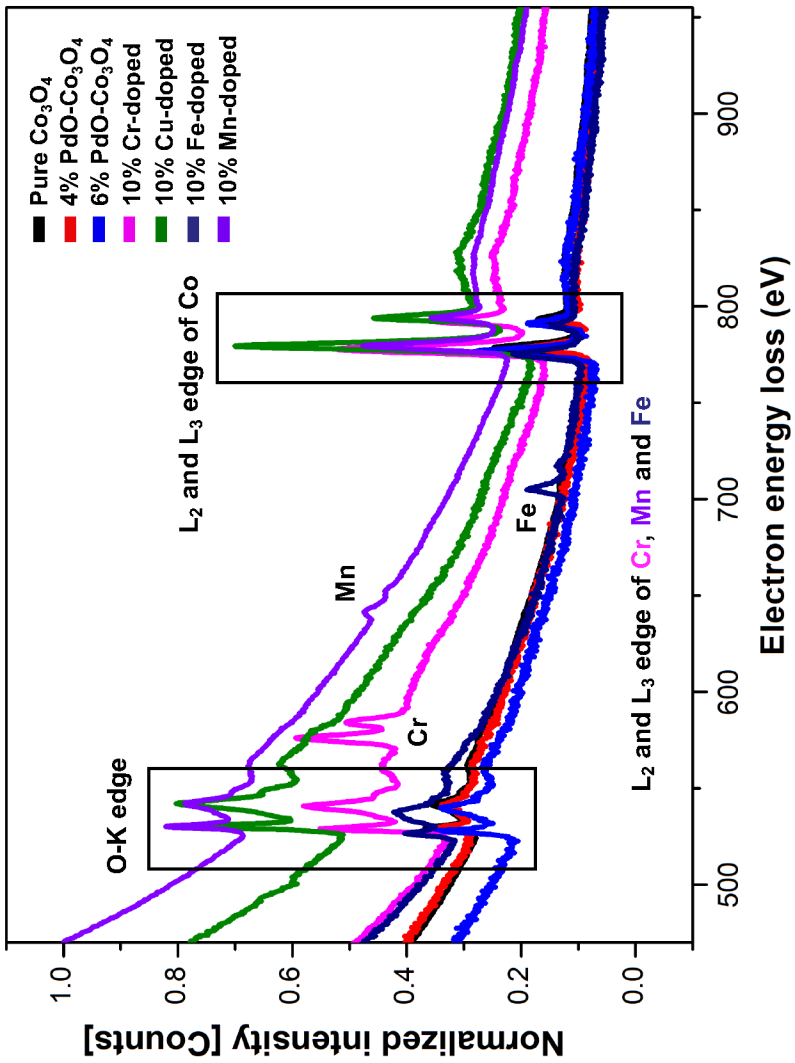
Pure Co_3O_4
4% PdO-Co_3O_4
6% PdO-Co_3O_4
10% Cr-doped
10% Cu-doped
10% Fe-doped
10% Mn-doped
O-K edge
L_2 and L_3 edge of Co
L_2 and L_3 edge of Cr, Mn and Fe
Mn
Cr
Fe
Normalized intensity [Counts]
Electron energy loss (eV)
0.0
0.2
0.4
0.6
0.8
1.0
500
600
700
800
900

Figure 1d

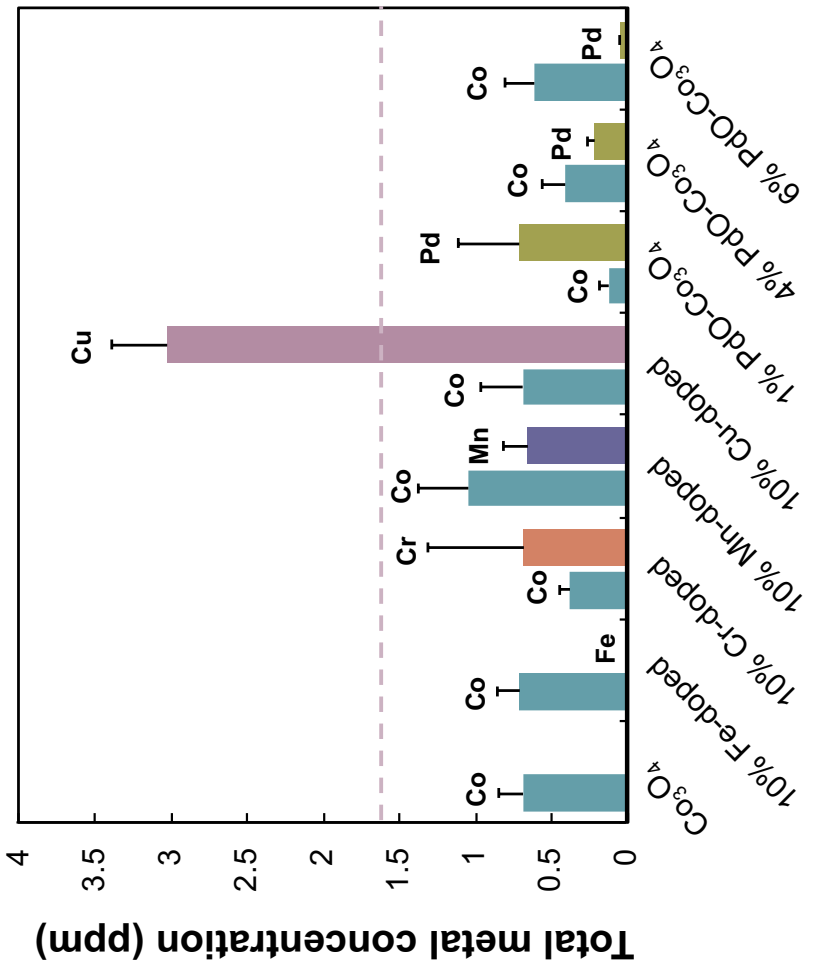
Total metal concentration (ppm)
0
0.5
1
1.5
2
2.5
3
3.5
4
Co3O4
10% Fe-doped
10% Cr-doped
10% Mn-doped
10% Cu-doped
1% PdO-Co3O4
4% PdO-Co3O4
6% PdO-Co3O4
Co
Fe
Co
Cr
Co
Mn
Co
Cu
Co
Pd
Co
Pd
Co
Pd

Figure 1e

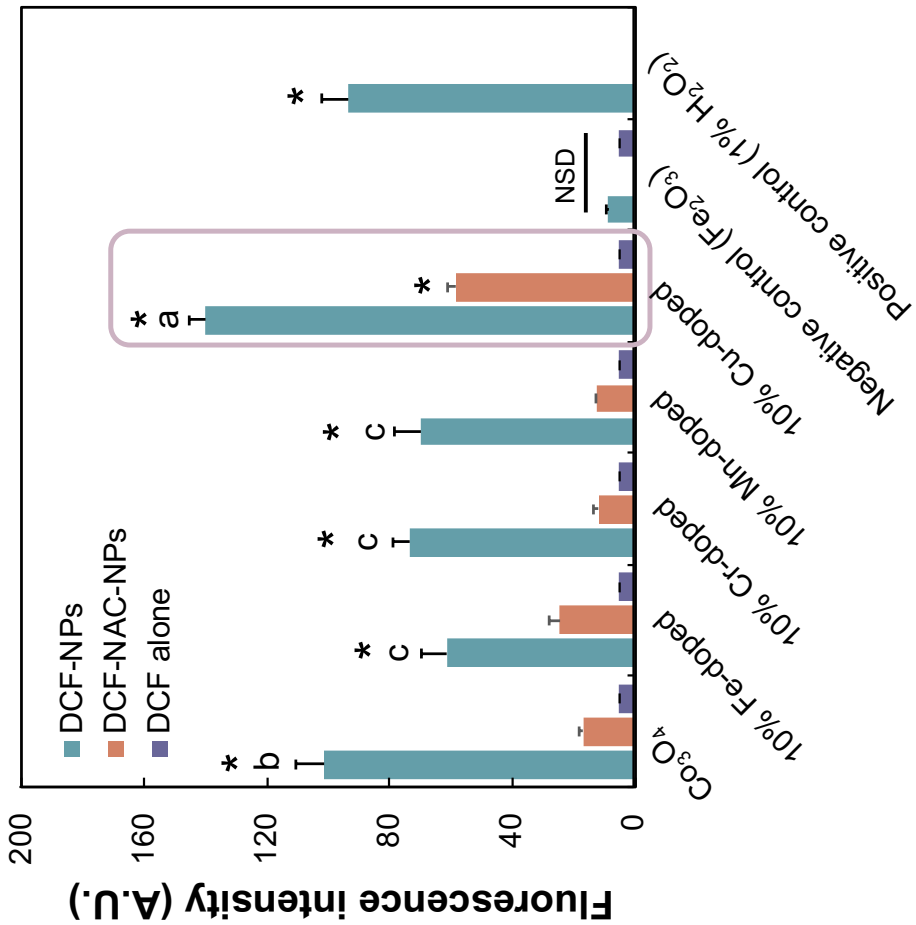
Fluorescence intensity (A.U.)
0
40
80
120
160
200
DCF-NPs
DCF-NAC-NPs
DCF alone
Co3O4
10% Fe-doped
10% Cr-doped
10% Mn-doped
10% Cu-doped
Negative control (Fe2O3)
Positive control (1% H2O2)
NSD
a
b
c
c
c
*

Figure 1f

Figure 1g

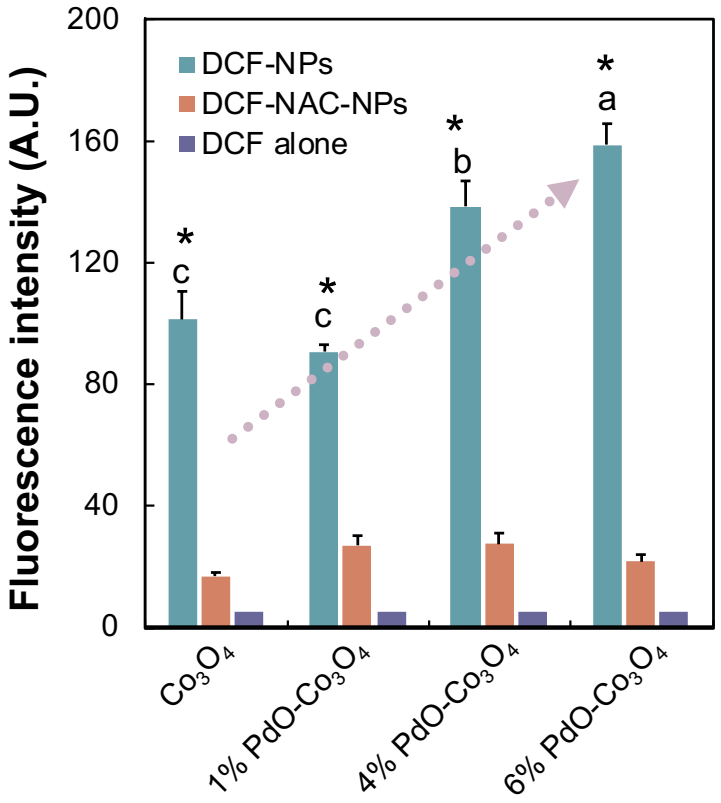
Fluorescence intensity (A.U.)
200
160
120
80
40
0
DCF-NPs
DCF-NAC-NPs
DCF alone
* c
* c
* b
* a
Co3O4
1% PdO-Co3O4
4% PdO-Co3O4
6% PdO-Co3O4

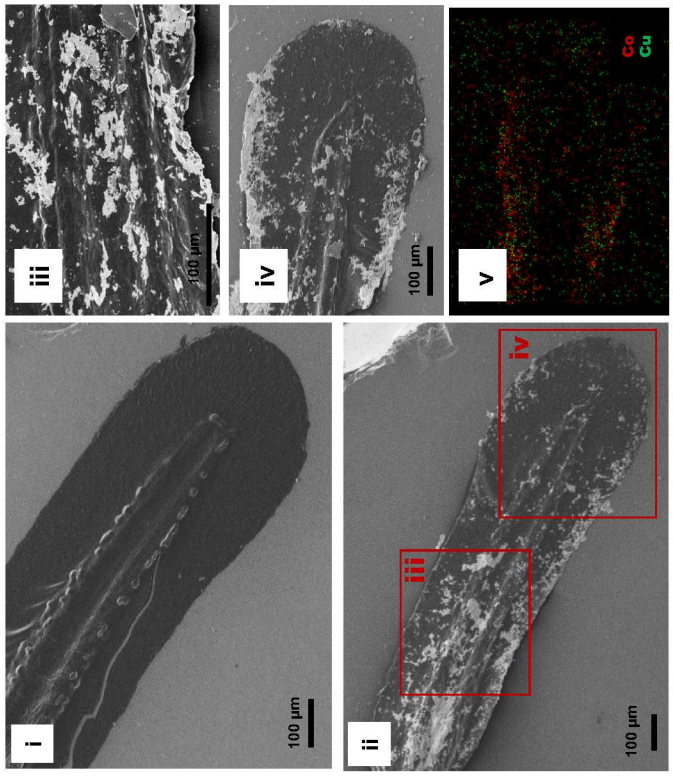

Figure 2a

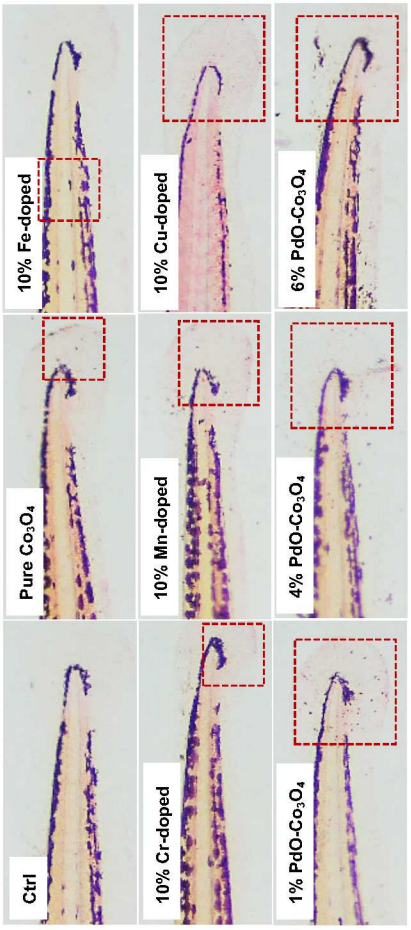

Co_3O_4-based nanoparticles	Control	Pure Co_3O_4	10% Fe-doped	10% Cr-doped	10% Mn-doped	10% Cu-doped	1% PdO-Co_3O_4	4% PdO-Co_3O_4	6% PdO-Co_3O_4
Injury level	-	+	+	+	++	+++	+++	+++	+++

Figure 2b

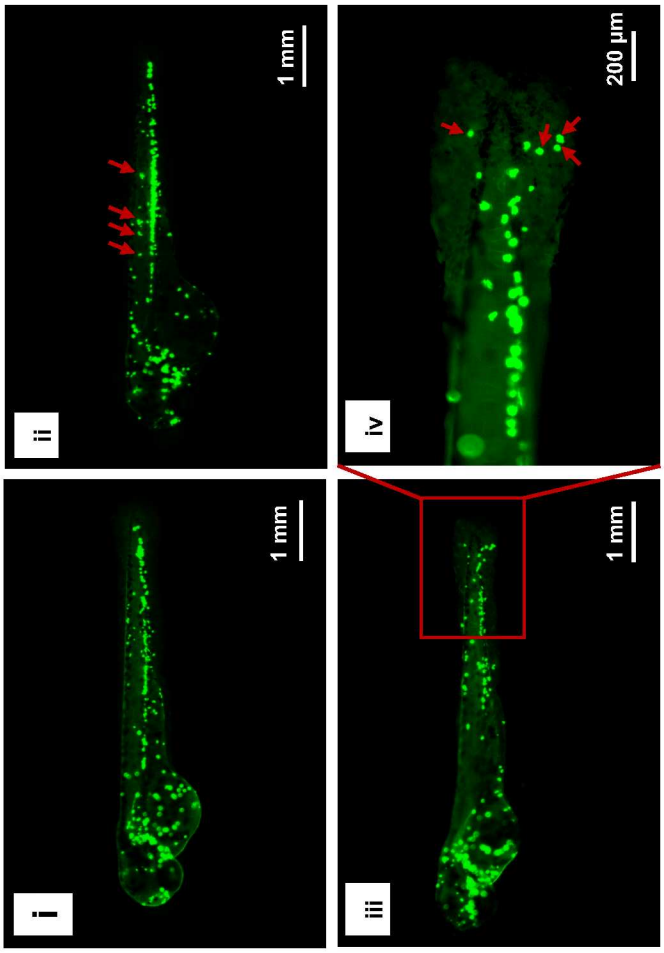

Figure 2c

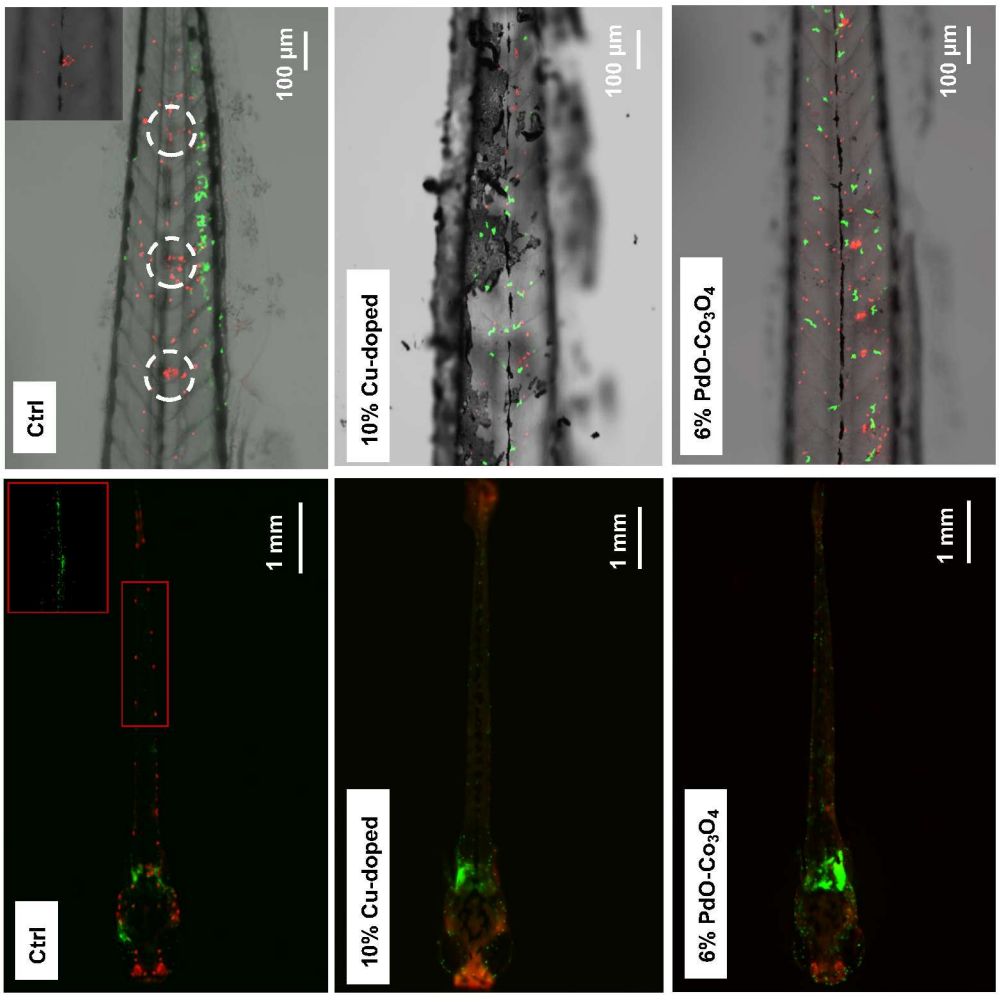
Ctrl
100 µm
10% Cu-doped
100 µm
6% PdO-Co3O4
100 µm
Ctrl
1 mm
10% Cu-doped
1 mm
6% PdO-Co3O4
1 mm

Figure 3a

Figure 3b

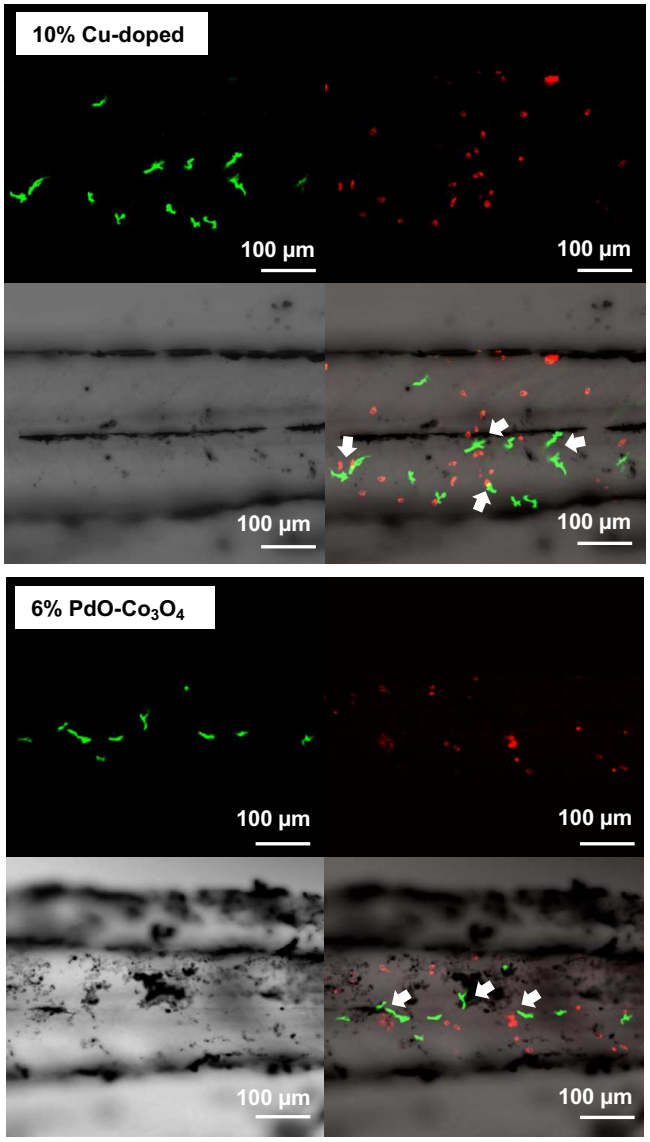
10% Cu-doped
100 μm
100 μm
100 μm
100 μm
6% PdO-Co3O4
100 μm
100 μm
100 μm
100 μm

Figure 4a

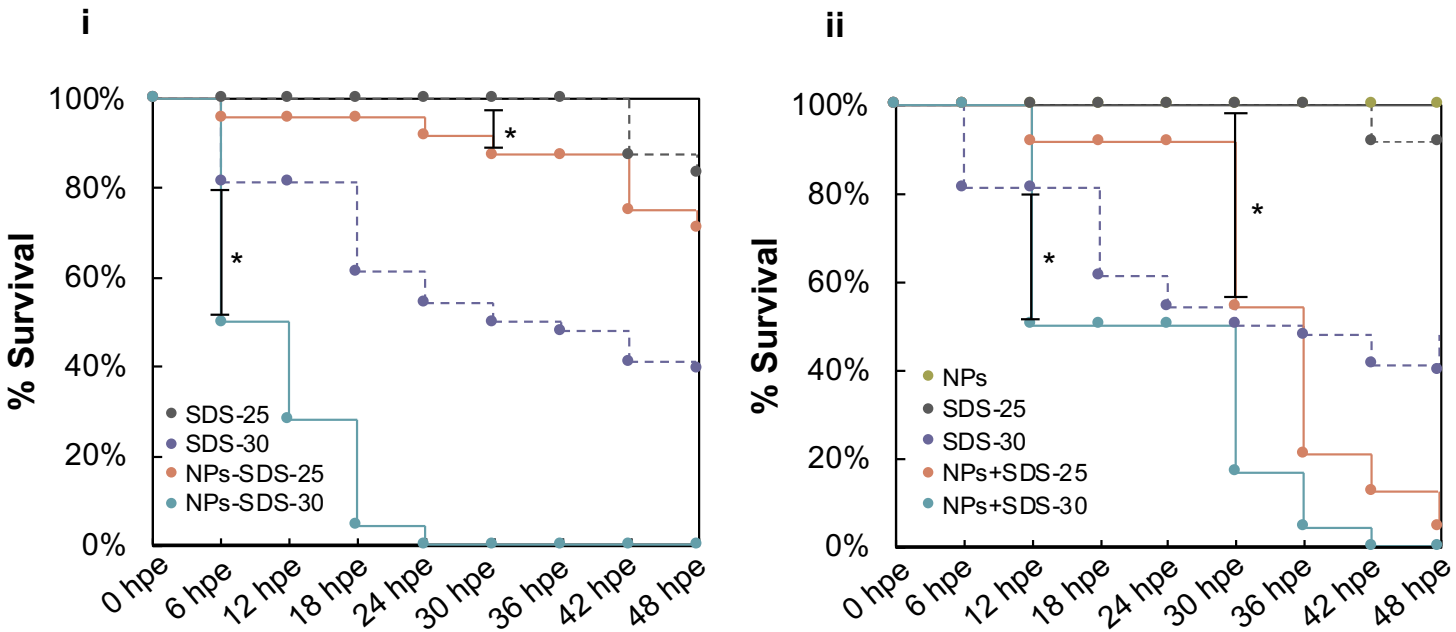
i
ii
% Survival
100%
80%
60%
40%
20%
0%
0 hpe
6 hpe
12 hpe
18 hpe
24 hpe
30 hpe
36 hpe
42 hpe
48 hpe
*
SDS-25
SDS-30
NPs-SDS-25
NPs-SDS-30
NPs
NPs+SDS-25
NPs+SDS-30

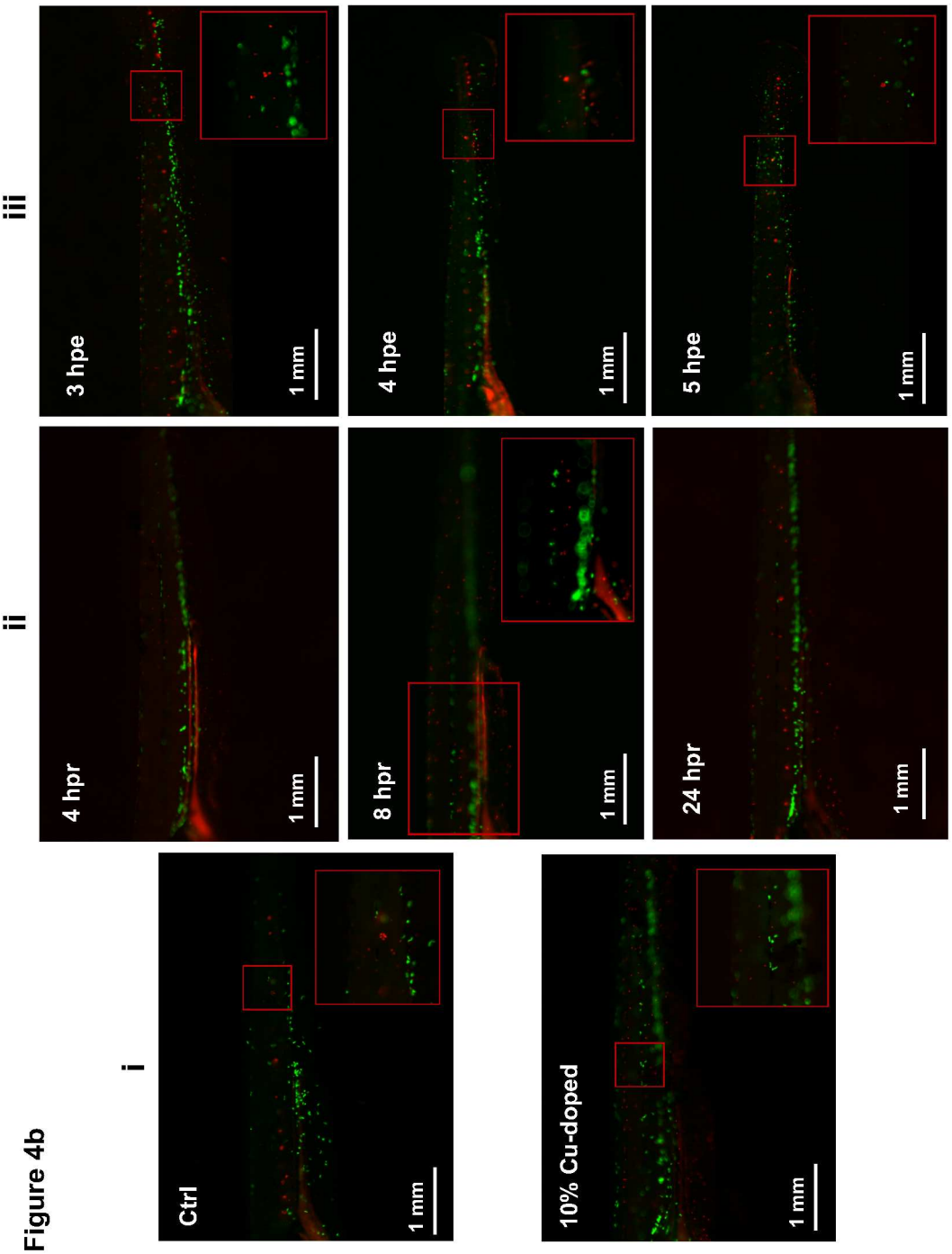

Figure 4b

Figure 5

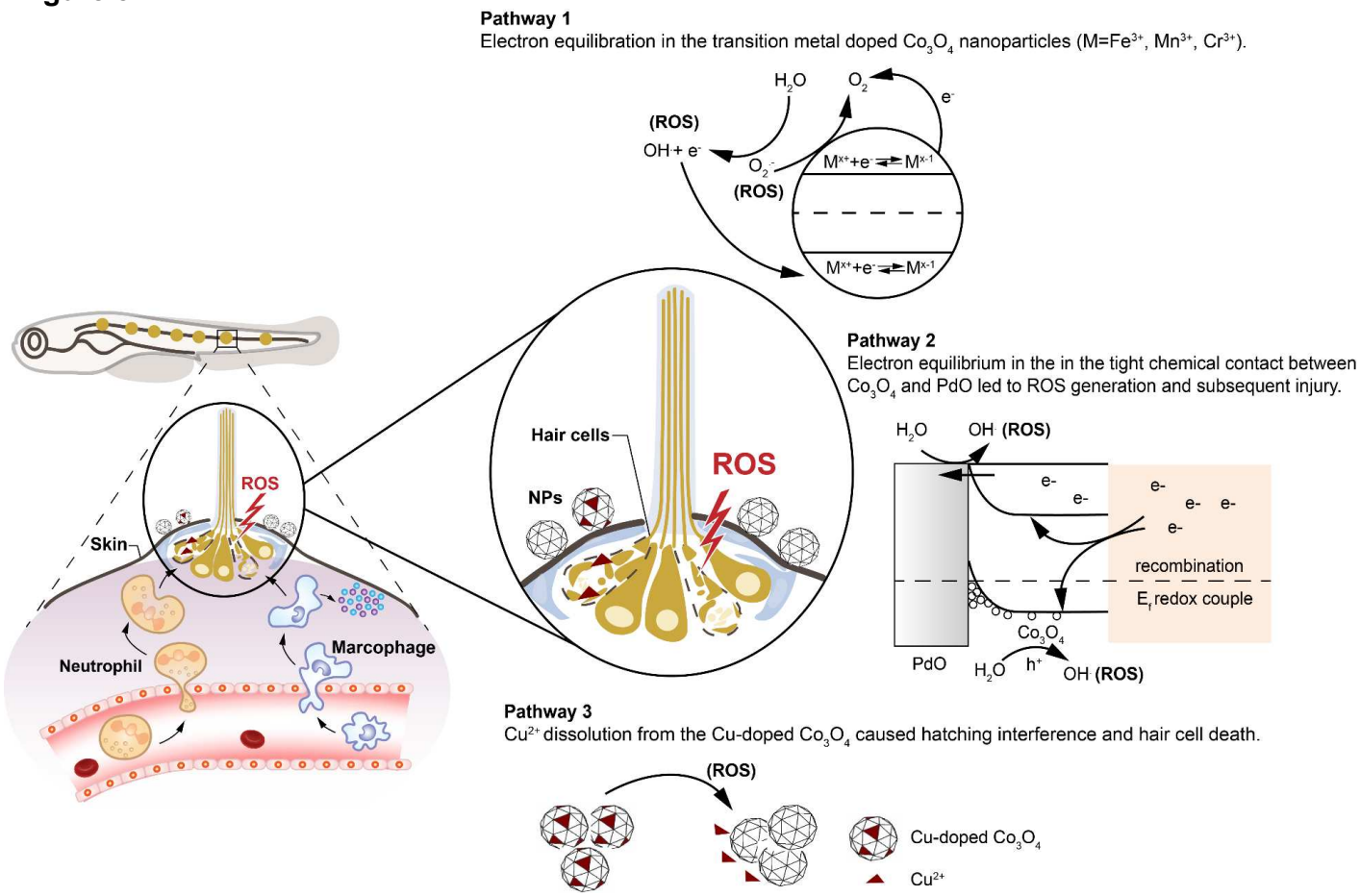
Pathway 1
Electron equilibration in the transition metal doped Co_3O_4 nanoparticles (M=Fe^{3+}, Mn^{3+}, Cr^{3+}).
H_2O
O_2
e^-
(ROS)
$OH + e^-$
O_2^-
(ROS)
$M^{x+}+e^- \rightleftharpoons M^{x-1}$
$M^{x+}+e^- \rightleftharpoons M^{x-1}$
Pathway 2
Electron equilibrium in the in the tight chemical contact between Co_3O_4 and PdO led to ROS generation and subsequent injury.
H_2O
OH (ROS)
e-
recombination
E_f redox couple
Co_3O_4
PdO
H_2O
h^+
OH (ROS)
Hair cells
NPs
ROS
ROS
Skin
Neutrophil
Marcophage
Pathway 3
Cu^{2+} dissolution from the Cu-doped Co_3O_4 caused hatching interference and hair cell death.
(ROS)
Cu-doped Co_3O_4
Cu^{2+}

Table 1

Co_3O_4 based nanoparticles	Surface area (m^2/g)	Particle size (d_{BET}) (nm)	Crystallite size (d_{XRD}) (nm)	Conduction band (eV)	Band gap energy (eV)	DLS (nm)	Zeta potential (mV)
Pure Co_3O_4	85.4	11.5	10.5	-4.61	2.56	85.0 ± 1.6	-8.2 ± 0.2
10% Fe	93.3	10.9	10.4	-4.45	2.82	112.3 ± 5.4	-6.4 ± 0.3
10% Cr	89.7	11.1	9.3	-4.49	2.73	93.2 ± 14.7	-1.0 ± 0.3
10% Mn	89.6	11.2	10.5	-4.47	2.77	85.3 ± 14.9	-1.2 ± 0.6
10% Cu	79.2	12.4	10.9	-4.45	2.84	119.7 ± 6.6	-13.0 ± 1.5
1% PdO	73.6	13.2	9.3	-4.50	2.78	116.1 ± 4.2	-10.5 ± 0.5
4% PdO	82.8	11.4	8.9	-4.51	2.76	122.8 ± 7.5	-9.8 ± 0.8
6% PdO	78.6	11.7	8.7	-4.52	2.74	109.7 ± 3.9	-10.4 ± 0.2